

Graph Neural Networks as Gradient Flows

Francesco Di Giovanni [†]
Twitter Inc.
fdigiovanni@twitter.com

James Rowbottom [†]
Twitter Inc.
jrowbottom@twitter.com

Benjamin P. Chamberlain
Twitter Inc.

Thomas Markovich
Twitter Inc.

Michael M. Bronstein
Twitter Inc. and University of Oxford

Abstract

Dynamical systems minimizing an energy are ubiquitous in geometry and physics. We propose a gradient flow framework for GNNs where the equations follow the direction of steepest descent of a learnable energy. This approach allows to explain the GNN evolution from a multi-particle perspective as learning attractive and repulsive forces in feature space via the positive and negative eigenvalues of a symmetric ‘channel-mixing’ matrix. We perform spectral analysis of the solutions and conclude that gradient flow graph convolutional models can induce a dynamics dominated by the graph high frequencies which is desirable for heterophilic datasets. We also describe structural constraints on common GNN architectures allowing to interpret them as gradient flows. We perform thorough ablation studies corroborating our theoretical analysis and show competitive performance of simple and lightweight models on real-world homophilic and heterophilic datasets.

1 Introduction and motivations

Graph neural networks (GNNs) [Sperduti \[1993\]](#), [Goller and Kuchler \[1996\]](#), [Gori et al. \[2005\]](#), [Scarselli et al. \[2008\]](#), [Bruna et al. \[2014\]](#), [Defferrard et al. \[2016\]](#), [Kipf and Welling \[2017\]](#), [Battaglia et al. \[2016, 2018\]](#) and in particular their Message Passing formulation (MPNN) [Gilmer et al. \[2017\]](#), [Brandstetter et al. \[2022\]](#) have become the standard ML tool for dealing with different types of relations and interactions, ranging from social networks to particle physics and drug design. One of the often cited drawbacks of traditional GNN models is their poor ‘explainability’, making it hard to know why and how they make certain predictions [Ying et al. \[2019\]](#), [Yuan et al. \[2020\]](#), and in which situations they may work and when they would fail. Limitations of GNNs that have attracted attention are over-smoothing [Nt and Maehara \[2019\]](#), [Oono and Suzuki \[2020\]](#), [Cai and Wang \[2020\]](#), over-squashing and bottlenecks [Alon and Yahav \[2021\]](#), [Topping et al. \[2022\]](#), and performance on heterophilic data [Pei et al. \[2020\]](#), [Zhu et al. \[2020\]](#), [Chien et al. \[2021\]](#), [Bo et al. \[2021\]](#), [Yan et al. \[2021\]](#) – where adjacent nodes usually have different labels.

Contributions. We propose a *Gradient Flow Framework* (GRAFF) where the GNN equations follow the direction of steepest descent of a *learnable energy*. Thanks to this framework we can (i) interpret GNNs as a multi-particle dynamics where the learned parameters determine pairwise attractive and repulsive potentials in the feature space. This sheds light on how GNNs can adapt to heterophily and explains their performance and the smoothness of the prediction. (ii) GRAFF leads to residual convolutional models where the *channel-mixing* \mathbf{W} is performed by a shared symmetric bilinear form inducing attraction and repulsion via its positive and negative eigenvalues, respectively. We theoretically investigate the interaction of the graph spectrum with the spectrum of the channel-mixing proving that if there is more mass on the negative eigenvalues of \mathbf{W} , then the dynamics

[†]Equal contribution

is dominated by the graph-high frequencies, which could be desirable on heterophilic graphs. We also extend results of [Nt and Maehara \[2019\]](#), [Oono and Suzuki \[2020\]](#), [Cai and Wang \[2020\]](#) by showing that when we drop the residual connection intrinsic to the gradient flow framework, graph convolutional models always induce a low-frequency dominated dynamics *independent* of the sign and magnitude of the spectrum of the channel-mixing. We also discuss how simple choices make common architectures fit GRAFF and conduct thorough ablation studies to corroborate the theoretical analysis on the role of the spectrum of \mathbf{W} . (iii) We crystallize *an instance* of our framework into a linear, residual, convolutional model that retains explainability and achieves competitive performance on homophilic and heterophilic real world graphs whilst being faster than GCN.

Related work. Our analysis is related to investigating GNNs as filters on the graph spectrum [Defferrard et al. \[2016\]](#), [Hammond et al. \[2019\]](#), [Balcilar et al. \[2020\]](#), [He et al. \[2021\]](#) and studying the over-smoothing effect [Nt and Maehara \[2019\]](#), [Oono and Suzuki \[2020\]](#), [Cai and Wang \[2020\]](#) and partly adopts techniques similar to [Oono and Suzuki \[2020\]](#). The key difference is that we also consider the spectrum of the ‘channel-mixing’ matrix. The concept of gradient flows has been a standard tool in physics and differential geometry [Eells and Sampson \[1964\]](#), from which they were adopted for image processing [Kimmel et al. \[1997\]](#), and more recently also used in ML [Sander et al. \[2022\]](#) for the analysis of Transformers [Vaswani et al. \[2017\]](#). Our continuous-time evolution equations follows the spirit of Neural ODES [Haber and Ruthotto \[2018\]](#), [Chen et al. \[2018\]](#), [Biloš et al. \[2021\]](#) and the study of GNNs as continuous dynamical systems [Xhonneux et al. \[2020\]](#), [Chamberlain et al. \[2021a\]](#), [Eliasof et al. \[2021\]](#), [Chamberlain et al. \[2021b\]](#), and more generally resonates with the geometric deep learning blueprint [Bronstein et al. \[2021\]](#), [Topping et al. \[2022\]](#), [Bodnar et al. \[2022\]](#), [Di Giovanni et al. \[2022\]](#).

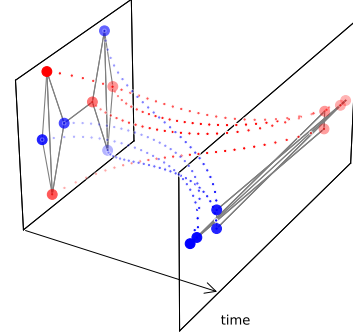


Figure 1: actual GRAFF dynamics: attractive and repulsive forces lead to a non-smoothing process able to separate labels.

Outline. In Section 2, we review the continuous and discrete Dirichlet energy and the associated gradient flow framework. We formalize the notion of over-smoothing and low(high)-frequency-dominated dynamics to investigate GNNs and study the dominant components in their evolution. We extend the graph Dirichlet energy to allow for a non-trivial norm for the feature edge-gradient. This leads to gradient flow equations that diffuse the features and over-smooth in the limit. Accordingly, in Section 3 we introduce a more general energy with a symmetric channel-mixing matrix \mathbf{W} giving rise to attractive and repulsive pairwise terms via its positive and negative eigenvalues and show that the negative spectrum can induce a high-frequency-dominant dynamics. In Section 4 we first compare with continuous GNN models and we then discretize the equations and provide a ‘recipe’ for making standard GNN architectures fit a gradient flow framework. We adapt the spectral analysis to discrete-time showing that gradient flow convolutional models *can* generate a dynamics dominated by the high frequencies via the negative eigenvalues of \mathbf{W} while this is impossible if we drop the residual connection. In Section 5 we corroborate our theoretical analysis on the role of the spectrum of \mathbf{W} via ablation studies on graphs with varying homophily. Experiments on real world datasets show a competitive performance of our model despite its simplicity and reduced number of parameters.

2 Gradient-flow formalism

Notations adopted throughout the paper. Let $G = (V, E)$ be an *undirected* graph with n nodes. We denote by $\mathbf{F} \in \mathbb{R}^{n \times d}$ the matrix of d -dimensional node features, by $\mathbf{f}_i \in \mathbb{R}^d$ its i -th row (transposed), by $\mathbf{f}^r \in \mathbb{R}^n$ its r -th column, and by $\text{vec}(\mathbf{F}) \in \mathbb{R}^{nd}$ the vectorization of \mathbf{F} obtained by stacking its columns. Given a symmetric matrix \mathbf{B} , we let $\lambda_+^{\mathbf{B}}, \lambda_-^{\mathbf{B}}$ denote its most positive and negative eigenvalues, respectively, and $\rho_{\mathbf{B}}$ be its *spectral radius*. If $\mathbf{B} \succeq 0$, then $\text{gap}(\mathbf{B})$ denotes the *positive smallest eigenvalue* of \mathbf{B} . $\dot{f}(t)$ denotes the temporal derivative, \otimes is the Kronecker product and ‘a.e.’ means *almost every* w.r.t. Lebesgue measure and usually refers to data in the complement of some lower dimensional subspace in $\mathbb{R}^{n \times d}$. Proofs and additional results appear in the Appendix.

Starting point: a geometric parallelism. To motivate a gradient-flow approach for GNNs, we start from the continuous case (see Appendix A.1 for details). Consider a smooth map $f : \mathbb{R}^n \rightarrow (\mathbb{R}^d, h)$

with h a constant metric represented by $\mathbf{H} \succeq 0$. The *Dirichlet energy* of f is defined by

$$\mathcal{E}(f, h) = \frac{1}{2} \int_{\mathbb{R}^n} \|\nabla f\|_h^2 dx = \frac{1}{2} \sum_{q,r=1}^d \sum_{j=1}^n \int_{\mathbb{R}^n} h_{qr} \partial_j f^q \partial_j f^r(x) dx \quad (1)$$

and measures the ‘smoothness’ of f . A natural approach to find minimizers of \mathcal{E} - called *harmonic maps* - was introduced in [Eells and Sampson \[1964\]](#) and consists in studying the **gradient flow** of \mathcal{E} , wherein a given map $f(0) = f_0$ is evolved according to $\dot{f}(t) = -\nabla_f \mathcal{E}(f(t))$. This type of evolution equations have historically been the core of *variational* and *PDE-based image processing*; in particular, gradient flows of the Dirichlet energy were shown [Kimmel et al. \[1997\]](#) to recover the Perona-Malik nonlinear diffusion [Perona and Malik \[1990\]](#).

Motivation: GNNs for node-classification. We wish to extend the gradient flow formalism to node classification on graphs. Assume we have a graph G , node-features \mathbf{F}_0 and labels $\{y_i\}$ on $V_{\text{tr}} \subset V$, and that we want to predict the labels on $V_{\text{test}} \subset V$. A GNN typically evolves the features via some parametric rule, $\text{GNN}_\theta(G, \mathbf{F}_0)$, and uses a decoding map for the prediction $y = \psi_{\text{DE}}(\text{GNN}_\theta(G, \mathbf{F}_0))$. In graph convolutional models [Defferrard et al. \[2016\]](#), [Kipf and Welling \[2017\]](#), GNN_θ consists of two operations: applying a shared linear transformation to the features (**‘channel mixing’**) and propagating them along the edges of the graph (**‘diffusion’**). Our **goal** consists in studying when GNN_θ is the *gradient flow* of some parametric class of energies $\mathcal{E}_\theta : \mathbb{R}^{n \times d} \rightarrow \mathbb{R}$, which generalize the Dirichlet energy. This means that the parameters can be interpreted as ‘finding the right notion of smoothness’ for our task. We evolve the features by $\dot{\mathbf{F}}(t) = -\nabla_{\mathbf{F}} \mathcal{E}_\theta(\mathbf{F}(t))$ with prediction $y = \psi_{\text{DE}}(\mathbf{F}(T))$ for some optimal time T .

Why a gradient flow? Since $\dot{\mathcal{E}}_\theta(\mathbf{F}(t)) = -\|\nabla_{\mathbf{F}} \mathcal{E}_\theta(\mathbf{F}(t))\|^2$, the energy dissipates along the gradient flow. Accordingly, this framework allows to *explain the GNN dynamics* as flowing the node features in the direction of steepest descent of \mathcal{E}_θ . Indeed, we find that parametrizing an energy leads to equations governed by attractive and repulsive forces that can be controlled via the spectrum of symmetric ‘channel-mixing’ matrices. This shows that by learning to distribute more mass over the negative (positive) eigenvalues of the channel-mixing, gradient flow models can generate dynamics dominated by the higher (respectively, lower) graph frequencies and hence tackle different homophily scenarios. The gradient flow framework also leads to sharing of the weights across layers (since we parametrize the *energy* rather than the *evolution equations*, as usually done in GNNs), allowing us to reduce the number of parameters without compromising performance (see [Table 1](#)).

Analysis on graphs: preliminaries. Given a *connected* graph G with self-loops, its adjacency matrix \mathbf{A} is defined as $a_{ij} = 1$ if $(i, j) \in E$ and zero otherwise. We let $\mathbf{D} = \text{diag}(d_i)$ be the degree matrix and write $\bar{\mathbf{A}} := \mathbf{D}^{-1/2} \mathbf{A} \mathbf{D}^{-1/2}$. Let $\mathbf{F} \in \mathbb{R}^{n \times d}$ be the matrix representation of a signal. Its *graph gradient* is $(\nabla \mathbf{F})_{ij} := \mathbf{f}_j / \sqrt{d_j} - \mathbf{f}_i / \sqrt{d_i}$. We define the *Laplacian* as $\Delta := -\frac{1}{2} \text{div } \nabla$ (the *divergence* div is the adjoint of ∇), represented by $\Delta = \mathbf{I} - \bar{\mathbf{A}} \succeq 0$. We refer to the eigenvalues of Δ as *frequencies*: the lowest frequency is always 0 while the highest frequency is $\rho_\Delta \leq 2$ [Chung and Graham \[1997\]](#). As for the continuum case, the gradient allows to define a (*graph*) *Dirichlet energy* as [Zhou and Schölkopf \[2005\]](#)

$$\mathcal{E}^{\text{Dir}}(\mathbf{F}) := \frac{1}{4} \sum_i \sum_{j:(i,j) \in E} \|(\nabla \mathbf{F})_{ij}\|^2 \equiv \frac{1}{4} \sum_{(i,j) \in E} \left\| \frac{\mathbf{f}_i}{\sqrt{d_i}} - \frac{\mathbf{f}_j}{\sqrt{d_j}} \right\|^2 = \frac{1}{2} \text{trace}(\mathbf{F}^\top \Delta \mathbf{F}), \quad (2)$$

where the extra $\frac{1}{2}$ is for convenience. As for manifolds, \mathcal{E}^{Dir} measures smoothness. If we stack the columns of \mathbf{F} into $\text{vec}(\mathbf{F}) \in \mathbb{R}^{nd}$, the gradient flow of \mathcal{E}^{Dir} yields the *heat equation* on each channel:

$$\text{vec}(\dot{\mathbf{F}}(t)) = -\nabla_{\text{vec}(\mathbf{F})} \mathcal{E}^{\text{Dir}}(\text{vec}(\mathbf{F}(t))) = -(\mathbf{I}_d \otimes \Delta) \text{vec}(\mathbf{F}(t)) \iff \dot{\mathbf{f}}^r(t) = -\Delta \mathbf{f}^r(t), \quad (3)$$

for $1 \leq r \leq d$. Similarly to [Cai and Wang \[2020\]](#), we rely on \mathcal{E}^{Dir} to assess whether a given dynamics $t \mapsto \mathbf{F}(t)$ is a smoothing process. A different choice of Laplacian $\mathbf{L} = \mathbf{D} - \mathbf{A}$ with non-normalized adjacency induces the analogous Dirichlet energy $\mathcal{E}_{\mathbf{L}}^{\text{Dir}}(\mathbf{F}) = \frac{1}{2} \text{trace}(\mathbf{F}^\top \mathbf{L} \mathbf{F})$. Throughout this paper, we rely on the following definitions (see [Appendix A.3](#) for further equivalent formulations and justifications):

Definition 2.1. $\dot{\mathbf{F}}(t) = \text{GNN}_\theta(\mathbf{F}(t), t)$ initialized at $\mathbf{F}(0)$ is *smoothing* if $\mathcal{E}^{\text{Dir}}(\mathbf{F}(t)) \leq C + \varphi(t)$, with C a constant only depending on $\mathcal{E}^{\text{Dir}}(\mathbf{F}(0))$ and $\dot{\varphi}(t) \leq 0$. *Over-smoothing* occurs if either $\mathcal{E}^{\text{Dir}}(\mathbf{F}(t)) \rightarrow 0$ or $\mathcal{E}_{\mathbf{L}}^{\text{Dir}}(\mathbf{F}(t)) \rightarrow 0$ for $t \rightarrow \infty$.

Our notion of ‘over-smoothing’ is a relaxed version of the definition in [Rusch et al. \[2022\]](#) – although in the linear case one always finds an *exponential decay* of \mathcal{E}^{Dir} . We note that $\mathcal{E}^{\text{Dir}}(\mathbf{F}(t)) \rightarrow 0$ iff $\Delta \mathbf{f}^r(t) \rightarrow \mathbf{0}$ for each column \mathbf{f}^r . As in [Oono and Suzuki \[2020\]](#), this corresponds to a loss of separation power along the solution where nodes with *equal degree* become indistinguishable since we converge to $\ker(\Delta)$ (if we replaced Δ with \mathbf{L} then we would not even be able to separate nodes with different degrees in the limit).

To motivate the next definition, consider $\dot{\mathbf{F}}(t) = \bar{\mathbf{A}}\mathbf{F}(t)$. Despite $\|\mathbf{F}(t)\|$ being unbounded for a.e. $\mathbf{F}(0)$, the low-frequency components are growing the fastest and indeed $\mathbf{F}(t)/\|\mathbf{F}(t)\| \rightarrow \mathbf{F}_\infty$ s.t. $\Delta \mathbf{f}_\infty^r = \mathbf{0}$ for $1 \leq r \leq d$. We formalize this scenario – including the opposite case of high-frequency components being dominant – by studying $\mathcal{E}^{\text{Dir}}(\mathbf{F}(t)/\|\mathbf{F}(t)\|)$, i.e. the Rayleigh quotient of $\mathbf{I}_d \otimes \Delta$.

Definition 2.2. $\dot{\mathbf{F}}(t) = \text{GNN}_\theta(\mathbf{F}(t), t)$ initialized at $\mathbf{F}(0)$ is *Low/High-Frequency-Dominant (L/HFD)* if $\mathcal{E}^{\text{Dir}}(\mathbf{F}(t)/\|\mathbf{F}(t)\|) \rightarrow 0$ (respectively, $\mathcal{E}^{\text{Dir}}(\mathbf{F}(t)/\|\mathbf{F}(t)\|) \rightarrow \rho_\Delta/2$) for $t \rightarrow \infty$.

We report a consequence of Definition 2.2 and refer to Appendix A.3 for additional details and motivations for the characterizations of LFD and HFD.

Lemma 2.3. GNN_θ is LFD (HFD) iff for each $t_j \rightarrow \infty$ there exist $t_{j_k} \rightarrow \infty$ and \mathbf{F}_∞ s.t. $\mathbf{F}(t_{j_k})/\|\mathbf{F}(t_{j_k})\| \rightarrow \mathbf{F}_\infty$ and $\Delta \mathbf{f}_\infty^r = \mathbf{0}$ ($\Delta \mathbf{f}_\infty^r = \rho_\Delta \mathbf{f}_\infty^r$, respectively).

If a graph is *homophilic*, adjacent nodes are likely to share the same label and we expect a smoothing or LFD dynamics enhancing the low-frequency components to be successful at node classification tasks [Wu et al. \[2019\]](#), [Klicpera et al. \[2019\]](#). In the opposite case of *heterophily*, the high-frequency components might contain more relevant information for separating classes [Bo et al. \[2021\]](#), [Bodnar et al. \[2022\]](#) – the prototypical example being the eigenvector of Δ associated with largest frequency ρ_Δ separating a regular bipartite graph. In other words, the class of heterophilic graphs contain instances where signals should be *sharpened* by increasing \mathcal{E}^{Dir} rather than smoothed out. Accordingly, an ideal framework for learning on graphs must accommodate both of these opposite scenarios by being able to induce either an LFD or a HFD dynamics.

Parametric Dirichlet energy: channel-mixing as metric in feature space. In eq. (1) a constant nontrivial metric h in \mathbb{R}^d leads to the mixing of the feature channels. We adapt this idea by considering a symmetric positive semi-definite $\mathbf{H} = \mathbf{W}^\top \mathbf{W}$ with $\mathbf{W} \in \mathbb{R}^{d \times d}$ and using it to generalize \mathcal{E}^{Dir} as

$$\mathcal{E}_{\mathbf{W}}^{\text{Dir}}(\mathbf{F}) := \frac{1}{4} \sum_{q,r=1}^d \sum_i \sum_{j:(i,j) \in \mathbf{E}} h_{qr}(\nabla \mathbf{F}^q)_{ij}(\nabla \mathbf{F}^r)_{ij} = \frac{1}{4} \sum_{(i,j) \in \mathbf{E}} \|\mathbf{W}(\nabla \mathbf{F})_{ij}\|^2. \quad (4)$$

We note the analogy with eq. (1), where the sum over the nodes replaces the integration over the domain and the j -th derivative at some point i is replaced by the gradient along the edge $(i, j) \in \mathbf{E}$. We generally treat \mathbf{W} as *learnable weights* and study the gradient flow of $\mathcal{E}_{\mathbf{W}}^{\text{Dir}}$:

$$\dot{\mathbf{F}}(t) = -\nabla_{\mathbf{F}} \mathcal{E}_{\mathbf{W}}^{\text{Dir}}(\mathbf{F}(t)) = -\Delta \mathbf{F}(t) \mathbf{W}^\top \mathbf{W}. \quad (5)$$

We see that eq. (5) generalizes eq. (3). Below ‘smoothing’ is intended as in Definition 2.1.

Proposition 2.4. Let $P_{\mathbf{W}}^{\ker}$ be the projection onto $\ker(\mathbf{W}^\top \mathbf{W})$. Equation (5) is smoothing since

$$\mathcal{E}^{\text{Dir}}(\mathbf{F}(t)) \leq e^{-2t \text{gap}(\mathbf{W}^\top \mathbf{W}) \text{gap}(\Delta)} \|\mathbf{F}(0)\|^2 + \mathcal{E}^{\text{Dir}}((P_{\mathbf{W}}^{\ker} \otimes \mathbf{I}_n) \text{vec}(\mathbf{F}(0))), \quad t \geq 0.$$

In fact $\mathbf{F}(t) \rightarrow \mathbf{F}_\infty$ s.t. $\exists \phi_\infty \in \mathbb{R}^d$: for each $i \in \mathbf{V}$ we have $(\mathbf{f}_\infty)_i = \sqrt{d_i} \phi_\infty + P_{\mathbf{W}}^{\ker} \mathbf{f}_i(0)$.

Proposition 2.4 implies that *no weight matrix \mathbf{W} in eq. (5) can separate the limit embeddings $\mathbf{F}(\infty)$ of nodes with same degree and input features*. If \mathbf{W} has a trivial kernel, then nodes with same degrees converge to the same representation and *over-smoothing* occurs as per Definition 2.1. Differently from [Nt and Maehara \[2019\]](#), [Oono and Suzuki \[2020\]](#), [Cai and Wang \[2020\]](#), over-smoothing occurs independently of the spectral radius of the ‘channel-mixing’ if its eigenvalues are *positive* – even for equations which lead to residual GNNs when discretized [Chen et al. \[2018\]](#). According to Proposition 2.4, we do not expect eq. (5) to succeed on heterophilic graphs where *smoothing* processes are generally harmful – this is confirmed in Figure 2 (see *prod-curve*). To remedy this problem, we generalize eq. (5) to a gradient flow that can be HFD as per Definition 2.2.

3 A general parametric energy for pairwise interactions

We extend the Dirichlet energy associated with $\mathbf{H} = \mathbf{W}^\top \mathbf{W} \succeq 0$ to an energy accounting for mutual – possibly repulsive – interactions in feature space \mathbb{R}^d . We first rewrite the energy $\mathcal{E}_{\mathbf{W}}^{\text{Dir}}$ in eq. (4) as

$$\mathcal{E}_{\mathbf{W}}^{\text{Dir}}(\mathbf{F}) = \frac{1}{2} \sum_i \langle \mathbf{f}_i, \mathbf{W}^\top \mathbf{W} \mathbf{f}_i \rangle - \frac{1}{2} \sum_{i,j} \bar{a}_{ij} \langle \mathbf{f}_i, \mathbf{W}^\top \mathbf{W} \mathbf{f}_j \rangle. \quad (6)$$

Replacing the occurrences of $\mathbf{W}^\top \mathbf{W}$ with symmetric matrices $\Omega, \mathbf{W} \in \mathbb{R}^{d \times d}$ leads to

$$\mathcal{E}^{\text{tot}}(\mathbf{F}) := \frac{1}{2} \sum_i \langle \mathbf{f}_i, \Omega \mathbf{f}_i \rangle - \frac{1}{2} \sum_{i,j} \bar{a}_{ij} \langle \mathbf{f}_i, \mathbf{W} \mathbf{f}_j \rangle \equiv \mathcal{E}_{\Omega}^{\text{ext}}(\mathbf{F}) + \mathcal{E}_{\mathbf{W}}^{\text{pair}}(\mathbf{F}), \quad (7)$$

with associated gradient flow of the form (see Appendix B)

$$\dot{\mathbf{F}}(t) = -\nabla_{\mathbf{F}} \mathcal{E}^{\text{tot}}(\mathbf{F}(t)) = -\mathbf{F}(t)\Omega + \bar{\mathbf{A}}\mathbf{F}(t)\mathbf{W}. \quad (8)$$

Note that eq. (8) is gradient flow of some energy $\mathbf{F} \mapsto \mathcal{E}^{\text{tot}}(\mathbf{F})$ iff both Ω and \mathbf{W} are symmetric.

A multi-particle system point of view: attraction vs repulsion. Consider the d -dimensional node-features as particles in \mathbb{R}^d with energy \mathcal{E}^{tot} . While the term $\mathcal{E}_{\Omega}^{\text{ext}}$ is *independent of the graph topology* and represents an **external** field in the feature space, the second term $\mathcal{E}_{\mathbf{W}}^{\text{pair}}$ constitutes a potential energy, with \mathbf{W} a *bilinear form* determining the **pairwise interactions** of adjacent node representations. Given a symmetric \mathbf{W} , we write $\mathbf{W} = \Theta_+^\top \Theta_+ - \Theta_-^\top \Theta_-$, by decomposing the spectrum of \mathbf{W} in positive and negative values. We can rewrite $\mathcal{E}^{\text{tot}} = \mathcal{E}_{\Omega - \mathbf{W}}^{\text{ext}} + \mathcal{E}_{\Theta_+}^{\text{Dir}} - \mathcal{E}_{\Theta_-}^{\text{Dir}}$, i.e.

$$\mathcal{E}^{\text{tot}}(\mathbf{F}) = \frac{1}{2} \sum_i \langle \mathbf{f}_i, (\Omega - \mathbf{W}) \mathbf{f}_i \rangle + \frac{1}{4} \sum_{i,j} \|\Theta_+(\nabla \mathbf{F})_{ij}\|^2 - \frac{1}{4} \sum_{i,j} \|\Theta_-(\nabla \mathbf{F})_{ij}\|^2. \quad (9)$$

The gradient flow of \mathcal{E}^{tot} *minimizes* $\mathcal{E}_{\Theta_+}^{\text{Dir}}$ and *maximizes* $\mathcal{E}_{\Theta_-}^{\text{Dir}}$. The matrix \mathbf{W} encodes *repulsive pairwise interactions* via its negative-definite component Θ_- which lead to terms $\|\Theta_-(\nabla \mathbf{F})_{ij}\|^2$ increasing along the solution. The latter affords a ‘sharpening’ effect desirable on heterophilic graphs where we need to disentangle adjacent node representations and hence ‘magnify’ the edge-gradient.

Spectral analysis of the channel-mixing. We will now show that eq. (8) can lead to a HFD dynamics. To this end, we assume that $\Omega = \mathbf{0}$ so that eq. (8) becomes $\dot{\mathbf{F}}(t) = \bar{\mathbf{A}}\mathbf{F}(t)\mathbf{W}$. According to eq. (9) the negative eigenvalues of \mathbf{W} lead to repulsion. We show that the latter can induce HFD dynamics as per Definition 2.2. We let $P_{\mathbf{W}}^{\rho_-}$ be the orthogonal projection into the eigenspace of $\mathbf{W} \otimes \bar{\mathbf{A}}$ associated with the eigenvalue $\rho_- := |\lambda_-^{\mathbf{W}}|(\rho_{\Delta} - 1)$. Moreover, we define

$$\epsilon_{\text{HFD}} := \min\{\rho_- - \lambda_+^{\mathbf{W}}, |\lambda_-^{\mathbf{W}}| \text{gap}(\rho_{\Delta} \mathbf{I} - \Delta), \text{gap}(|\lambda_-^{\mathbf{W}}| \mathbf{I} + \mathbf{W})(\rho_{\Delta} - 1)\}.$$

Proposition 3.1. *If $\rho_- > \lambda_+^{\mathbf{W}}$, then $\dot{\mathbf{F}}(t) = \bar{\mathbf{A}}\mathbf{F}(t)\mathbf{W}$ is HFD for a.e. $\mathbf{F}(0)$: we have*

$$\mathcal{E}^{\text{Dir}}(\mathbf{F}(t)) = e^{2t\rho_-} \left(\frac{\rho_{\Delta}}{2} \|P_{\mathbf{W}}^{\rho_-} \mathbf{F}(0)\|^2 + \mathcal{O}(e^{-2t\epsilon_{\text{HFD}}}) \right), \quad t \geq 0,$$

and $\mathbf{F}(t)/\|\mathbf{F}(t)\|$ converges to $\mathbf{F}_{\infty} \in \mathbb{R}^{n \times d}$ such that $\Delta \mathbf{f}_{\infty}^r = \rho_{\Delta} \mathbf{f}_{\infty}^r$, for $1 \leq r \leq d$.

Proposition 3.1 shows that *if enough mass of the spectrum of the ‘channel-mixing’ is distributed over the negative eigenvalues, then the evolution is dominated by the graph high frequencies*. This analysis is made possible in our gradient flow framework where \mathbf{W} must be *symmetric*. The HFD dynamics induced by negative eigenvalues of \mathbf{W} is confirmed in Figure 2 (*neg-prod-curve* in the bottom chart).

A more general energy. Equations with a source term may have better expressive power [Xhonneux et al. \[2020\]](#), [Chen et al. \[2020\]](#), [Thorpe et al. \[2021\]](#). In our framework this means adding an extra energy term of the form $\mathcal{E}_{\tilde{\mathbf{W}}}^{\text{source}}(\mathbf{F}) := \beta \langle \mathbf{F}, \mathbf{F}(0) \tilde{\mathbf{W}} \rangle$ to eq. (7) with some learnable β and $\tilde{\mathbf{W}}$. This leads to the following gradient flow:

$$\dot{\mathbf{F}}(t) = -\mathbf{F}(t)\Omega + \bar{\mathbf{A}}\mathbf{F}(t)\mathbf{W} - \beta \mathbf{F}(0) \tilde{\mathbf{W}}. \quad (10)$$

We also observe that one could replace the fixed matrix $\bar{\mathbf{A}}$ with a more general *symmetric graph vector field* \mathcal{A} satisfying $\mathcal{A}_{ij} = 0$ if $(i, j) \notin E$. This in particular includes the case where $\mathcal{A} = \mathcal{A}(\mathbf{F}(0))$ is

learned based on the initial encoding via an *attention* mechanism Vaswani et al. [2017], Veličković et al. [2018]. In this case, the pairwise energy generalizes to

$$\mathcal{E}_{\mathcal{A}, \mathbf{W}}^{\text{pair}}(\mathbf{F}) := -\sum_{(i,j)} \mathcal{A}_{ij} \langle \mathbf{f}_i, \mathbf{W}\mathbf{f}_j \rangle. \quad (11)$$

Since in the experiments we have not observed improvements from learning \mathcal{A} and this option does make the model slower, we stick to the special choice $\mathcal{A} = \bar{\mathbf{A}}$. We also note that when $\Omega = \mathbf{W}$, then eq. (8) becomes $\dot{\mathbf{F}}(t) = -\Delta \mathbf{F}(t) \mathbf{W}$. We perform a spectral analysis of this case in Appendix B.2.

Non-linear activations. The inner products in the formulations of $\mathcal{E}_{\Omega}^{\text{ext}}$, $\mathcal{E}_{\mathbf{W}}^{\text{pair}}$ can be combined with non-linear activations σ of the form (the gradient flow derivation is reported in Appendix B.3)

$$\mathcal{E}_{\Omega}^{\text{ext}}(\mathbf{F}) + \mathcal{E}_{\mathbf{W}}^{\text{pair}}(\mathbf{F}) = \frac{1}{2} \sum_i \sigma(\langle \mathbf{f}_i, \Omega \mathbf{f}_i \rangle) - \frac{1}{2} \sum_{i,j} \bar{a}_{ij} \sigma(\langle \mathbf{f}_i, \mathbf{W}\mathbf{f}_j \rangle).$$

While non-linear activations offer greater expressive power, the analysis presented thus far and the following comparisons with existing GNN models are investigated in the linear case for a few reasons. First, in the spirit of Wu et al. [2019], Oono and Suzuki [2020], Chen et al. [2020], by dropping non-linear maps we can perform spectral analysis in closed form. Second, in all our experiments we have seen no gain in performance when including non-linear activations. Third, we can always ‘push the non-linear maps’ in either the encoding block or the decoding one without affecting the linear gradient flow as discussed in Section 4.

4 Comparison with GNNs

In this Section, we study standard GNN models from the perspective of our gradient flow framework.

4.1 Continuous case

Continuous GNN models replace layers with continuous time. In contrast with Proposition 3.1, we show that three main *linearized* continuous GNN models are either *smoothing* or LFD as per Definition 2.2. The linearized PDE-GCN_D model Eliasof et al. [2021] corresponds to choosing $\beta = 0$ and $\Omega = \mathbf{W} = \mathbf{K}(t)^\top \mathbf{K}(t)$ in eq. (10), for some time-dependent family $t \mapsto \mathbf{K}(t) \in \mathbb{R}^{d \times d}$:

$$\dot{\mathbf{F}}_{\text{PDE-GCN}_D}(t) = -\Delta \mathbf{F}(t) \mathbf{K}(t)^\top \mathbf{K}(t).$$

The CGNN model Xhonneux et al. [2020] can be derived from eq. (10) by setting $\Omega = \mathbf{I} - \tilde{\Omega}$, $\mathbf{W} = \tilde{\mathbf{W}} = \mathbf{I}$, $\beta = 1$:

$$\dot{\mathbf{F}}_{\text{CGNN}}(t) = -\Delta \mathbf{F}(t) + \mathbf{F}(t) \tilde{\Omega} + \mathbf{F}(0).$$

Finally, in linearized GRAND Chamberlain et al. [2021a] a row-stochastic matrix $\mathcal{A}(\mathbf{F}(0))$ is *learned* from the encoding via an attention mechanism and we have

$$\dot{\mathbf{F}}_{\text{GRAND}}(t) = -\Delta_{\text{RW}} \mathbf{F}(t) = -(\mathbf{I} - \mathcal{A}(\mathbf{F}(0))) \mathbf{F}(t).$$

We note that if \mathcal{A} is not symmetric, then GRAND is *not* a gradient flow.

Proposition 4.1. PDE – GCN_D, CGNN and GRAND satisfy the following:

- (i) PDE – GCN_D is a *smoothing model*: $\dot{\mathcal{E}}^{\text{Dir}}(\mathbf{F}_{\text{PDE-GCN}_D}(t)) \leq 0$.
- (ii) For a.e. $\mathbf{F}(0)$ it holds: CGNN is never HFD and if we remove the source term, then $\mathcal{E}^{\text{Dir}}(\mathbf{F}_{\text{CGNN}}(t)/\|\mathbf{F}_{\text{CGNN}}(t)\|) \leq e^{-\text{gap}(\Delta)t}$.
- (iii) If G is connected, $\mathbf{F}_{\text{GRAND}}(t) \rightarrow \boldsymbol{\mu}$ as $t \rightarrow \infty$, with $\boldsymbol{\mu}^r = \text{mean}(\mathbf{f}^r(0))$, $1 \leq r \leq d$.

By (ii) the source-free CGNN-evolution is LFD *independent of* $\tilde{\Omega}$. Moreover, by (iii), over-smoothing occurs for GRAND as per Definition 2.1. On the other hand, Proposition 3.1 shows that the negative eigenvalues of \mathbf{W} can make the source-free gradient flow in eq. (8) HFD. Experiments in Section 5 confirm that the gradient flow model outperforms CGNN and GRAND on heterophilic graphs.

4.2 Discrete case

We now describe a discrete version of our gradient flow model and compare it to ‘discrete’ GNNs where discrete time steps correspond to different layers. In the spirit of [Chen et al. \[2018\]](#), we use explicit Euler scheme with step size $\tau \leq 1$ to solve eq. (10) and set $\tilde{\mathbf{W}} = \mathbf{I}$. In the gradient flow framework we *parametrize the energy* rather than the actual equations, which leads to *symmetric* channel-mixing matrices $\Omega, \mathbf{W} \in \mathbb{R}^{d \times d}$ that are *shared across the layers*. Since the matrices are square, an *encoding* block $\psi_{\text{EN}} : \mathbb{R}^{n \times p} \rightarrow \mathbb{R}^{n \times d}$ is used to process input features $\mathbf{F}_0 \in \mathbb{R}^{n \times p}$ and generally reduce the hidden dimension from p to d . Moreover, the iterations inherently lead to a residual architecture because of the explicit Euler discretization:

$$\mathbf{F}(t + \tau) = \mathbf{F}(t) + \tau \left(-\mathbf{F}(t)\Omega + \bar{\mathbf{A}}\mathbf{F}(t)\mathbf{W} + \beta\mathbf{F}(0) \right), \quad \mathbf{F}(0) = \psi_{\text{EN}}(\mathbf{F}_0), \quad (12)$$

with prediction $y = \psi_{\text{DE}}(\mathbf{F}(T))$ produced by a *decoder* $\psi_{\text{DE}} : \mathbb{R}^{n \times d} \rightarrow \mathbb{R}^{n \times k}$, where k is the number of label classes and T *integration time* of the form $T = m\tau$, so that $m \in \mathbb{N}$ represents the number of *layers*. Although eq. (12) is linear, we can include non-linear activations in $\psi_{\text{EN}}, \psi_{\text{DE}}$. Until this point, we have considered equations that minimize a multi-particle energy. We now study when GNNs minimize an energy $\mathcal{E}^{\text{tot}} = \mathcal{E}_{\Omega}^{\text{ext}} + \mathcal{E}_{\mathbf{A}, \mathbf{W}}^{\text{pair}} + \mathcal{E}_{\tilde{\mathbf{W}}}^{\text{source}}$.

Are discrete GNNs gradient flows? Given a (learned) symmetric graph vector field $\mathcal{A} \in \mathbb{R}^{n \times n}$ satisfying $\mathcal{A}_{ij} = 0$ if $(i, j) \notin E$, consider a family of linear GNNs with shared weights of the form

$$\mathbf{F}(t + 1) = \mathbf{F}(t)\Omega + \mathcal{A}\mathbf{F}(t)\mathbf{W} + \beta\mathbf{F}(0)\tilde{\mathbf{W}}, \quad 0 \leq t \leq T. \quad (13)$$

Symmetry is the key requirement to interpret GNNs in eq. (13) in a gradient flow framework.

Lemma 4.2. *Equation (13) is the unit step size discrete gradient flow of $\mathcal{E}_{\mathbf{I}-\Omega}^{\text{ext}} + \mathcal{E}_{\mathbf{A}, \mathbf{W}}^{\text{pair}} - \mathcal{E}_{\tilde{\mathbf{W}}}^{\text{source}}$, with $\mathcal{E}_{\mathbf{A}, \mathbf{W}}^{\text{pair}}$ defined in eq. (11), iff Ω and \mathbf{W} are symmetric.*

Lemma 4.2 provides a recipe for making standard architectures into a gradient flow, with *symmetry* being the key requirement. When eq. (13) is a gradient flow, the underlying GNN dynamics becomes *explainable* in terms of minimizing a multi-particle energy by learning attractive and repulsive directions in feature space as discussed in Section 3. In Appendix C.2, we show how Lemma 4.2 covers linear versions of GCN [Kipf and Welling \[2017\]](#), Wu et al. [2019], GAT [Veličković et al. \[2018\]](#), GraphSAGE [Hamilton et al. \[2017\]](#) and GCNII [Chen et al. \[2020\]](#) to name a few.

Over-smoothing analysis in discrete setting. By Proposition 3.1 we know that the continuous version of eq. (12) can be HFD thanks to the negative eigenvalues of \mathbf{W} . The next result represents a discrete counterpart of Proposition 3.1 and shows that *residual, symmetrized graph convolutional models can be HFD*. Below $P_{\mathbf{W}}^{\rho_-}$ is the projection into the eigenspace associated with the eigenvalue $\rho_- := |\lambda_{-}^{\mathbf{W}}|(\rho_{\Delta} - 1)$ and we report the explicit value of δ_{HFD} in eq. (29) in Appendix C.3. We let:

$$\lambda_{+}^{\mathbf{W}}(\rho_{\Delta} - 1)^{-1} < |\lambda_{-}^{\mathbf{W}}| < 2(\tau(2 - \rho_{\Delta}))^{-1}. \quad (14)$$

Theorem 4.3. *Given $\mathbf{F}(t + \tau) = \mathbf{F}(t) + \tau\bar{\mathbf{A}}\mathbf{F}(t)\mathbf{W}$, with \mathbf{W} symmetric, if eq. (14) holds then*

$$\mathcal{E}^{\text{Dir}}(\mathbf{F}(m\tau)) = (1 + \tau\rho_-)^{2m} \left(\frac{\rho_{\Delta}}{2} \|P_{\mathbf{W}}^{\rho_-} \mathbf{F}(0)\|^2 + \mathcal{O} \left(\left(\frac{1 + \tau\delta_{\text{HFD}}}{1 + \tau\rho_-} \right)^{2m} \right) \right), \quad \delta_{\text{HFD}} < \rho_-,$$

hence the dynamics is HFD for a.e. $\mathbf{F}(0)$ and in fact $\mathbf{F}(m\tau)/\|\mathbf{F}(m\tau)\| \rightarrow \mathbf{F}_{\infty}$ s.t. $\Delta\mathbf{f}_{\infty}^r = \rho_{\Delta}\mathbf{f}_{\infty}^r$. Conversely, if G is not bipartite, then for a.e. $\mathbf{F}(0)$ the system $\mathbf{F}(t + \tau) = \tau\bar{\mathbf{A}}\mathbf{F}(t)\mathbf{W}$, with \mathbf{W} symmetric, is LFD independent of the spectrum of \mathbf{W} .

Theorem 4.3 shows that linear discrete gradient flows can be HFD due to the negative eigenvalues of \mathbf{W} . This differs from statements that standard GCNs act as low-pass filters and thus over-smooth in the limit. Indeed, in these cases the spectrum of \mathbf{W} is generally ignored [Wu et al. \[2019\]](#), [Chen et al. \[2020\]](#) or required to be sufficiently small in terms of singular value decomposition [Nt and Maehara \[2019\]](#), [Oono and Suzuki \[2020\]](#), [Cai and Wang \[2020\]](#) when no residual connection is present. On the other hand, Theorem 4.3 emphasizes that the spectrum of \mathbf{W} plays a key role to enhance the high frequencies when enough mass is distributed over the negative eigenvalues provided that a residual connection exists – this is confirmed by the *neg-prod*-curve in Figure 2.

The residual connection from a spectral perspective. Given a sufficiently small step-size so that the right hand side of inequality 14 is satisfied, $\mathbf{F}(t + \tau) = \mathbf{F}(t) + \tau \mathbf{A} \mathbf{F}(t) \mathbf{W}$ is HFD for a.e. $\mathbf{F}(0)$ if $|\lambda_-^{\mathbf{W}}|(\rho_{\Delta} - 1) > \lambda_+^{\mathbf{W}}$, i.e. ‘there is more mass’ in the negative spectrum of \mathbf{W} than in the positive one. This means that differently from Nt and Maehara [2019], Oono and Suzuki [2020], Cai and Wang [2020], there is no requirement on the minimal magnitude of the spectral radius of \mathbf{W} coming from the graph topology as long as $\lambda_+^{\mathbf{W}}$ is small enough. Conversely, without a residual term, the dynamics is LFD for a.e. $\mathbf{F}(0)$ *independently* of the sign and magnitude of the eigenvalues of \mathbf{W} . This is also confirmed by the GCN-curve in Figure 2.

Gradient flow as spectral GNNs. We finally discuss eq. (12) from the perspective of spectral GNNs as in Balcilar et al. [2020]. Let us assume that $\beta = 0, \Omega = \mathbf{0}$. We can write eq. (12) as (see Appendix C.3)

$$\mathbf{f}^r(t + \tau) = \sum_{q=1}^d \mathbf{U}(\delta_{qr} \mathbf{I} + \tau W_{qr}(\mathbf{I} - \mathbf{\Lambda})) \mathbf{U}^{\top} \mathbf{f}^q(t), \quad 1 \leq r \leq d, \quad (15)$$

with $\mathbf{\Lambda} = \mathbf{U} \mathbf{\Lambda} \mathbf{U}^{\top}$ the eigendecomposition of the graph Laplacian. Namely, if we let $\{\lambda_r^{\mathbf{W}}\}$ be the spectrum of \mathbf{W} with associated orthonormal basis of eigenvectors given by $\{\phi_r^{\mathbf{W}}\}$, and we introduce $\mathbf{z}^r(t) : \mathcal{V} \rightarrow \mathbb{R}$ defined by $z_i^r(t) = \langle \mathbf{f}_i(t), \phi_r^{\mathbf{W}} \rangle$, then we can rephrase eq. (15) as the system

$$\mathbf{z}^r(t + \tau) = \mathbf{U}(\mathbf{I} + \tau \lambda_r^{\mathbf{W}}(\mathbf{I} - \mathbf{\Lambda})) \mathbf{U}^{\top} \mathbf{z}^r(t) = \mathbf{z}^r(t) + \tau \lambda_r^{\mathbf{W}} \bar{\mathbf{A}} \mathbf{z}^r(t), \quad 1 \leq r \leq d. \quad (16)$$

Accordingly, for each projection into the r -th eigenvector of \mathbf{W} , we have a spectral function in the graph frequency domain given by $\lambda^{\Delta} \mapsto 1 + \tau \lambda_r^{\mathbf{W}}(1 - \lambda^{\Delta})$. If $\lambda_r^{\mathbf{W}} > 0$ we have a *low-pass* filter while if $\lambda_r^{\mathbf{W}} < 0$ we have a *high-pass* filter. Moreover, we see that along the eigenvectors of \mathbf{W} , if $\lambda_r^{\mathbf{W}} < 0$ then the dynamics is equivalent to flipping the sign of the edge weights, which offers a direct comparison with methods proposed in Bo et al. [2021], Yan et al. [2021] where some ‘attentive’ mechanism is proposed to learn negative edge weights based on feature information. The very same procedure of changing the sign of the edge weights – which is *equivalent to reversing the time orientation for the evolution of \mathbf{z}^r* – can indeed be accomplished via the repulsive forces generated by the negative spectrum of \mathbf{W} .

5 Experiments

In this section we evaluate the gradient flow framework (GRAFF). We corroborate the spectral analysis using synthetic data with controllable homophily. We confirm that having negative (positive) eigenvalues of the channel-mixing \mathbf{W} are essential in heterophilic (homophilic) scenarios where the gradient flow should align with HFD (LFD) respectively. We show that the gradient flow in eq. (12) – a linear, residual, symmetric graph convolutional model – achieves competitive performance on real world datasets.

Methodology. We crystallize GRAFF in the model presented in eq. (12) with $\psi_{\text{EN}}, \psi_{\text{DE}}$ implemented as single linear layers or MLPs, and we set Ω to be diagonal. For the real-world experiments we consider *diagonally-dominant* (DD), *diagonal* (D) and *time-dependent* choices for the structure of \mathbf{W} that offer explicit control over its spectrum. In the (DD)-case, we consider a $\mathbf{W}^0 \in \mathbb{R}^{d \times d}$ *symmetric* with zero diagonal and $\mathbf{w} \in \mathbb{R}^d$ defined by $w_{\alpha} = q_{\alpha} \sum_{\beta} |\mathbf{W}_{\alpha\beta}^0| + r_{\alpha}$, and set $\mathbf{W} = \text{diag}(\mathbf{w}) + \mathbf{W}^0$. Due to the Gershgorin Theorem the eigenvalues of \mathbf{W} belong to $[\mathbf{w}_{\alpha} - \sum_{\beta} |\mathbf{W}_{\alpha\beta}^0|, \mathbf{w}_{\alpha} + \sum_{\beta} |\mathbf{W}_{\alpha\beta}^0|]$, so the model ‘can’ easily re-distribute mass in the spectrum of \mathbf{W} via q_{α}, r_{α} . This generalizes the decomposition of \mathbf{W} in Chen et al. [2020] providing a justification in terms of its spectrum and turns out to be more efficient w.r.t. the hidden dimension d as shown in Figure 4 in the Appendix. For (D) we take \mathbf{W} to be diagonal, with entries sampled $\mathcal{U}[-1, 1]$ and fixed – i.e., **we do not train** over \mathbf{W} – and only learn $\psi_{\text{EN}}, \psi_{\text{DE}}$. We also include a *time-dependent* model where \mathbf{W}_t varies across layers. To investigate the role of the spectrum of \mathbf{W} on synthetic graphs, we construct three additional variants: $\mathbf{W} = \mathbf{W}' + \mathbf{W}'^{\top}$, $\mathbf{W} = \pm \mathbf{W}'^{\top} \mathbf{W}'$ named *sum*, *prod* and *neg-prod* respectively where *prod* (*neg-prod*) variants have only non-negative (non-positive) eigenvalues.

Complexity and number of parameters. If we treat the number of layers as a constant, the discrete gradient flow scales as $\mathcal{O}(|V|pd + |E|d^2)$, where p and d are input feature and hidden dimension respectively, with $p \geq d$ usually. Note that GCN has complexity $\mathcal{O}(|E|pd)$ and in fact *our model is faster than GCN* as confirmed in Figure 5 in Appendix D. Since ψ_{EN}, ψ_{DE} are single linear layers (MLPs), we can bound the number of parameters by $pd + d^2 + 3d + dk$, with k the number of label classes, in the (DD)-variant while in the (D)-variant we have $pd + 3d + dk$. Further ablation studies appear in Figure 4 in the Appendix showing that (DD) outperforms *sum* and GCN – especially in the lower hidden dimension regime – on real-world benchmarks with varying homophily.

Synthetic experiments and ablation studies.

To investigate our claims in a controlled environment we use the synthetic Cora dataset of [Zhu et al., 2020, Appendix G]. Graphs are generated for target levels of homophily via preferential attachment – see Appendix D.3 for details. Figure 2 confirms the spectral analysis and offers *explainability* in terms of performance and smoothness of the predictions. Each curve – except GCN – represents one version of \mathbf{W} as in ‘methodology’ and we implement eq. (12) with $\beta = 0, \Omega = \mathbf{0}$. Figure 2 (top) reports the test accuracy vs true label homophily. *Neg-prod* is better than *prod* on low-homophily and viceversa on high-homophily. This confirms Proposition 3.1 where we have shown that the gradient flow can lead to a HFD dynamics – that are generally desirable with low-homophily – through the negative eigenvalues of \mathbf{W} . Conversely, the *prod* configuration (where we have an attraction-only dynamics) struggles in low-homophily scenarios *even though a residual connection is present*. Both *prod* and *neg-prod* are ‘extreme’ choices and serve the purpose of highlighting that by turning off one side of the spectrum this could be the more damaging depending on the underlying homophily. In general though ‘neutral’ variants like *sum* and (DD) are indeed more flexible and better performing. In fact, (DD) outperforms GCN especially in low-homophily scenarios, confirming Theorem 4.3 where we have shown that without a residual connection convolutional models are LFD – and hence more sensitive to underlying homophily – irrespectively of the spectrum of \mathbf{W} . This is further confirmed by additional ablation studies in Figure 3.

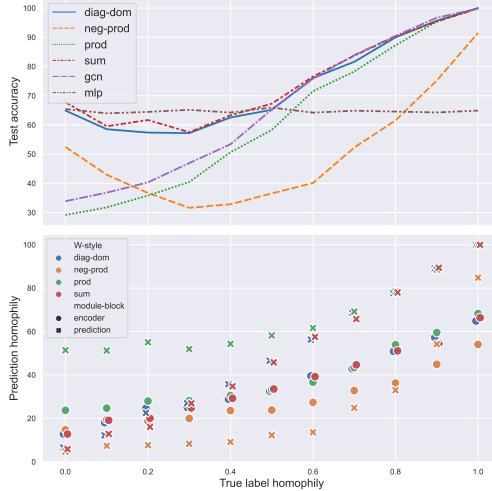


Figure 2: Experiments on synthetic datasets with controlled homophily.

In Figure 2 (bottom) we compute the homophily of the prediction (cross) for a given method and we compare with the homophily (circle) of the prediction read from the encoding (i.e. *graph-agnostic*). The homophily here is a proxy to assess whether the evolution is *smoothing*, the goal being explaining the smoothness of the prediction via the spectrum of \mathbf{W} as per our theoretical analysis. For *neg-prod* the homophily after the evolution is lower than that of the encoding, supporting the analysis that negative eigenvalues of \mathbf{W} enhance high-frequencies. The opposite behaviour occurs in the case of *prod* and explains that in the low-homophily regime *prod* is under-performant due to the prediction being smoother than the true homophily. (DD) and *sum* variants adapt better to the true homophily. We note how the encoding compensates when the dynamics can only either attract or repulse (i.e. the spectrum of \mathbf{W} has a sign) by decreasing or increasing the initial homophily respectively.

Real world experiments. We test GRAFF against a range of datasets with varying homophily Sen et al. [2008], Rozemberczki et al. [2021], Pei et al. [2020] (see Appendix D.4 for additional details). We use results provided in [Yan et al., 2021, Table 1], which includes standard baselines as GCN Kipf and Welling [2017], GraphSAGE Hamilton et al. [2017], GAT Veličković et al. [2018], PairNorm Zhao and Akoglu [2019] and recent models tailored towards the heterophilic setting (GGCN Yan et al. [2021], Geom-GCN Pei et al. [2020], H2GCN Zhu et al. [2020] and GPRGNN Chien et al. [2021]). For Sheaf Bodnar et al. [2022], a recent top-performer on heterophilic datasets, we took the best performing variant (out of six provided) for each dataset. We also include continuous baselines CGNN Xhonneux et al. [2020] and GRAND Chamberlain et al. [2021a] to provide empirical evidence for Proposition 4.1. Splits taken from Pei et al. [2020] are used in all the comparisons. The

	Texas	Wisconsin	Cornell	Film	Squirrel	Chameleon	Citeseer	Pubmed	Cora
Hom level	0.11	0.21	0.30	0.22	0.22	0.23	0.74	0.80	0.81
#Nodes	183	251	183	7,600	5,201	2,277	3,327	18,717	2,708
#Edges	295	466	280	26,752	198,493	31,421	4,676	44,327	5,278
#Classes	5	5	5	5	5	5	7	3	6
GGCN	84.86 ± 4.55	86.86 ± 3.29	85.68 ± 6.63	37.54 ± 1.56	55.17 ± 1.58	71.14 ± 1.84	77.14 ± 1.45	89.15 ± 0.37	87.95 ± 1.05
GPRGNN	78.38 ± 4.36	82.94 ± 4.21	80.27 ± 8.11	34.63 ± 1.22	31.61 ± 1.24	46.58 ± 1.71	77.13 ± 1.67	87.54 ± 0.38	87.95 ± 1.18
H2GCN	84.86 ± 7.23	87.65 ± 4.98	82.70 ± 5.28	35.70 ± 1.00	36.48 ± 1.86	60.11 ± 2.15	77.11 ± 1.57	89.49 ± 0.38	87.87 ± 1.20
GCNII	77.57 ± 3.83	80.39 ± 3.40	77.86 ± 3.79	37.44 ± 1.30	38.47 ± 1.58	63.86 ± 3.04	77.33 ± 1.48	90.15 ± 0.43	88.37 ± 1.25
Geom-GCN	66.76 ± 2.72	64.51 ± 3.66	60.54 ± 3.67	31.59 ± 1.15	38.15 ± 0.92	60.00 ± 2.81	78.02 ± 1.15	89.95 ± 0.47	85.35 ± 1.57
PairNorm	60.27 ± 4.34	48.43 ± 6.14	58.92 ± 3.15	27.40 ± 1.24	50.44 ± 2.04	62.74 ± 2.82	73.59 ± 1.47	87.53 ± 0.44	85.79 ± 1.01
GraphSAGE	82.43 ± 6.14	81.18 ± 5.56	75.95 ± 5.01	34.23 ± 0.99	41.61 ± 0.74	58.73 ± 1.68	76.04 ± 1.30	88.45 ± 0.50	86.90 ± 1.04
GCN	55.14 ± 5.16	51.76 ± 3.06	60.54 ± 5.30	27.32 ± 1.10	53.43 ± 2.01	64.82 ± 2.24	76.50 ± 1.36	88.42 ± 0.50	86.98 ± 1.27
GAT	52.16 ± 6.63	49.41 ± 4.09	61.89 ± 5.05	27.44 ± 0.89	40.72 ± 1.55	60.26 ± 2.50	76.55 ± 1.23	87.30 ± 1.10	86.33 ± 0.48
MLP	80.81 ± 4.75	85.29 ± 3.31	81.89 ± 6.40	36.53 ± 0.70	28.77 ± 1.56	46.21 ± 2.99	74.02 ± 1.90	75.69 ± 2.00	87.16 ± 0.37
CGNN	71.35 ± 4.05	74.31 ± 7.26	66.22 ± 7.69	35.95 ± 0.86	29.24 ± 1.09	46.89 ± 1.66	76.91 ± 1.81	87.70 ± 0.49	87.10 ± 1.35
GRAND	75.68 ± 7.25	79.41 ± 3.64	82.16 ± 7.09	35.62 ± 1.01	40.05 ± 1.50	54.67 ± 2.54	76.46 ± 1.77	89.02 ± 0.51	87.36 ± 0.96
Sheaf (max)	85.95 ± 5.51	89.41 ± 4.74	84.86 ± 4.71	37.81 ± 1.15	56.34 ± 1.32	68.04 ± 1.58	76.70 ± 1.57	89.49 ± 0.40	86.90 ± 1.13
GRAFF (DD)	88.38 ± 4.53	87.45 ± 2.94	83.24 ± 6.49	36.09 ± 0.81	54.52 ± 1.37	71.08 ± 1.75	76.92 ± 1.70	88.95 ± 0.52	87.61 ± 0.97
GRAFF (D)	88.11 ± 5.57	88.83 ± 3.29	84.05 ± 6.10	37.11 ± 1.08	47.36 ± 1.89	66.78 ± 1.28	77.30 ± 1.85	90.04 ± 0.41	88.01 ± 1.03
GRAFF-timedep (DD)	87.03 ± 4.49	87.06 ± 4.04	82.16 ± 7.07	35.93 ± 1.23	53.97 ± 1.45	69.56 ± 1.20	76.59 ± 1.53	88.26 ± 0.41	87.38 ± 1.05

Table 1: Results on heterophilic and homophilic datasets

GRAFF model discussed in ‘methodology’ is a very simple architecture with shared parameters across layers and run-time smaller than GCN and more recent models like GGCN designed for heterophilic graphs (see Figure 5 in the Appendix). Nevertheless, it achieves competitive results on all datasets, performing on par or better than more complex recent models. Moreover, comparison with the ‘time-dependent’ (DD) variant confirms that by sharing weights across layers we do not lose performance. We note that on heterophilic graphs short integration time is usually needed due to the topology being harmful and the negative eigenvalues of \mathbf{W} leading to exponential behaviour (see Appendix D).

6 Conclusions

In this work, we developed a framework for explainable GNNs where the evolution can be interpreted as minimizing a multi-particle learnable energy. This translates into studying the interaction between the spectrum of the graph and the spectrum of the ‘channel-mixing’ leading to a better understanding of when and why the induced dynamics is low (high) frequency dominated. From a theoretical perspective, we refined existing asymptotic analysis of GNNs to account for the role of the spectrum of the channel-mixing as well. From a practical perspective, our framework allows for ‘educated’ choices resulting in a simple, more explainable convolutional model that achieves competitive performance on homophilic and heterophilic benchmarks while being faster than GCN. Our results refute the folklore of graph convolutional models being too simple for complex benchmarks.

Limitations and future works. We limited our attention to a *constant* bilinear form \mathbf{W} , which might be excessively rigid. It is possible to derive non-constant alternatives that are *aware* of the features or the position in the graph. The main challenge amounts to matching the requirement for local ‘heterogeneity’ with efficiency: we reserve this question for future work. Our analysis is also a first step into studying the interaction of the graph and ‘channel-mixing’ spectra; we did not explore other dynamics that are neither LFD nor HFD as per our definitions. The energy formulation points to new models more ‘physics’ inspired; this will be explored in future work.

Societal impact. Our work sheds light on the actual dynamics of GNNs and could hence improve their explainability, which is crucial for assessing their impact on large-scale applications. We also show that instances of our framework achieve competitive performance on heterophilic data despite being faster than GCN, providing evidence for efficient methods with reduced footprint.

References

- Uri Alon and Eran Yahav. On the bottleneck of graph neural networks and its practical implications. In *International Conference on Learning Representations*, 2021. URL <https://openreview.net/forum?id=i800Ph0CVH2>.
- Muhammet Balçilar, Guillaume Renton, Pierre Héroux, Benoit Gaüzère, Sébastien Adam, and Paul Honeine. Analyzing the expressive power of graph neural networks in a spectral perspective. In *International Conference on Learning Representations*, 2020.
- Peter Battaglia, Razvan Pascanu, Matthew Lai, Danilo Jimenez Rezende, et al. Interaction networks for learning about objects, relations and physics. *Advances in neural information processing systems*, 29, 2016.
- Peter W Battaglia, Jessica B Hamrick, Victor Bapst, Alvaro Sanchez-Gonzalez, Vinicius Zambaldi, Mateusz Malinowski, Andrea Tacchetti, David Raposo, Adam Santoro, Ryan Faulkner, et al. Relational inductive biases, deep learning, and graph networks. *arXiv preprint arXiv:1806.01261*, 2018.
- Lukas Biewald. Experiment tracking with weights and biases, 2020. URL <https://www.wandb.com/>. Software available from wandb.com.
- Marin Biloš, Johanna Sommer, Syama Sundar Rangapuram, Tim Januschowski, and Stephan Günnemann. Neural flows: Efficient alternative to neural odes. In *Advances in Neural Information Processing Systems*, volume 34, 2021. URL <https://proceedings.neurips.cc/paper/2021/file/b21f9f98829dea9a48fd8aaddc1f159d-Paper.pdf>.
- Deyu Bo, Xiao Wang, Chuan Shi, and Huawei Shen. Beyond low-frequency information in graph convolutional networks. In *AAAI*. AAAI Press, 2021.
- Cristian Bodnar, Francesco Di Giovanni, Benjamin Paul Chamberlain, Pietro Liò, and Michael M Bronstein. Neural sheaf diffusion: A topological perspective on heterophily and oversmoothing in gns. *arXiv preprint arXiv:2202.04579*, 2022.
- Johannes Brandstetter, Daniel Worrall, and Max Welling. Message passing neural pde solvers. *arXiv preprint arXiv:2202.03376*, 2022.
- Michael M Bronstein, Joan Bruna, Taco Cohen, and Petar Veličković. Geometric deep learning: Grids, groups, graphs, geodesics, and gauges. *arXiv preprint arXiv:2104.13478*, 2021.
- Joan Bruna, Wojciech Zaremba, Arthur Szlam, and Yann LeCun. Spectral networks and locally connected networks on graphs. In *2nd International Conference on Learning Representations, ICLR 2014*, 2014.
- Chen Cai and Yusu Wang. A note on over-smoothing for graph neural networks. *arXiv preprint arXiv:2006.13318*, 2020.
- Ben Chamberlain, James Rowbottom, Maria I Gorinova, Michael Bronstein, Stefan Webb, and Emanuele Rossi. Grand: Graph neural diffusion. In *International Conference on Machine Learning*, pages 1407–1418. PMLR, 2021a.
- Benjamin Chamberlain, James Rowbottom, Davide Eynard, Francesco Di Giovanni, Xiaowen Dong, and Michael Bronstein. Beltrami flow and neural diffusion on graphs. *Advances in Neural Information Processing Systems*, 34, 2021b.
- Ming Chen, Zhewei Wei, Zengfeng Huang, Bolin Ding, and Yaliang Li. Simple and deep graph convolutional networks. In *International Conference on Machine Learning*, pages 1725–1735. PMLR, 2020.
- Ricky TQ Chen, Yulia Rubanova, Jesse Bettencourt, and David K Duvenaud. Neural ordinary differential equations. *Advances in neural information processing systems*, 31, 2018.
- Eli Chien, Jianhao Peng, Pan Li, and Olgica Milenkovic. Adaptive universal generalized pagerank graph neural network. In *9th International Conference on Learning Representations, ICLR 2021*, 2021. URL <https://openreview.net/forum?id=n6jl7fLxrP>.

- Fan RK Chung and Fan Chung Graham. Spectral graph theory. (92), 1997.
- Michaël Defferrard, Xavier Bresson, and Pierre Vandergheynst. Convolutional neural networks on graphs with fast localized spectral filtering. *Advances in neural information processing systems*, 29, 2016.
- Francesco Di Giovanni, Giulia Luise, and Michael Bronstein. Heterogeneous manifolds for curvature-aware graph embedding. *arXiv preprint arXiv:2202.01185*, 2022.
- James Eells and Joseph H Sampson. Harmonic mappings of riemannian manifolds. *American journal of mathematics*, 86(1):109–160, 1964.
- Moshe Eliasof, Eldad Haber, and Eran Treister. Pde-gcn: Novel architectures for graph neural networks motivated by partial differential equations. *Advances in Neural Information Processing Systems*, 34, 2021.
- Matthias Fey and Jan E. Lenssen. Fast graph representation learning with PyTorch Geometric. In *ICLR Workshop on Representation Learning on Graphs and Manifolds*, 2019.
- Justin Gilmer, Samuel S Schoenholz, Patrick F Riley, Oriol Vinyals, and George E Dahl. Neural message passing for quantum chemistry. In *International Conference on Machine Learning*, pages 1263–1272. PMLR, 2017.
- Christoph Goller and Andreas Kuchler. Learning task-dependent distributed representations by backpropagation through structure. In *Proceedings of International Conference on Neural Networks (ICNN’96)*, volume 1, pages 347–352. IEEE, 1996.
- Marco Gori, Gabriele Monfardini, and Franco Scarselli. A new model for learning in graph domains. In *Proceedings. 2005 IEEE International Joint Conference on Neural Networks, 2005.*, volume 2, pages 729–734. IEEE, 2005.
- E. Haber and L. Ruthotto. Stable architectures for deep neural networks. *Inverse Problems*, 34, 2018.
- Will Hamilton, Zhitao Ying, and Jure Leskovec. Inductive representation learning on large graphs. *Advances in neural information processing systems*, 30, 2017.
- David K Hammond, Pierre Vandergheynst, and Rémi Gribonval. The spectral graph wavelet transform: Fundamental theory and fast computation. In *Vertex-Frequency Analysis of Graph Signals*, pages 141–175. Springer, 2019.
- Mingguo He, Zhewei Wei, Hongteng Xu, et al. Bernnet: Learning arbitrary graph spectral filters via bernstein approximation. *Advances in Neural Information Processing Systems*, 34, 2021.
- Ron Kimmel, Nir Sochen, and Ravi Malladi. From high energy physics to low level vision. In *International Conference on Scale-Space Theories in Computer Vision*, pages 236–247. Springer, 1997.
- Thomas N. Kipf and Max Welling. Semi-Supervised Classification with Graph Convolutional Networks. In *Proceedings of the 5th International Conference on Learning Representations, ICLR ’17*, 2017. URL <https://openreview.net/forum?id=SJU4ayYgl>.
- Johannes Klicpera, Stefan Weissenberger, and Stephan Günnemann. Diffusion improves graph learning. In *Proceedings of the 33rd International Conference on Neural Information Processing Systems*, 2019.
- Hoang Nt and Takanori Maehara. Revisiting graph neural networks: All we have is low-pass filters. *arXiv preprint arXiv:1905.09550*, 2019.
- Kenta Oono and Taiji Suzuki. Graph neural networks exponentially lose expressive power for node classification. In *International Conference on Learning Representations*, 2020.
- Adam Paszke, Sam Gross, Francisco Massa, Adam Lerer, James Bradbury, Gregory Chanan, Trevor Killeen, Zeming Lin, Natalia Gimelshein, Luca Antiga, Alban Desmaison, Andreas Kopf, Edward Yang, Zachary DeVito, Martin Raison, Alykhan Tejani, Sasank Chilamkurthy, Benoit Steiner, Lu Fang, Junjie Bai, and Soumith Chintala. Pytorch: An imperative style, high-performance deep learning library. In *NeurIPS*, 2019.

- Hongbin Pei, Bingzhe Wei, Kevin Chen-Chuan Chang, Yu Lei, and Bo Yang. Geom-gcn: Geometric graph convolutional networks. In *8th International Conference on Learning Representations, ICLR 2020*, 2020.
- Pietro Perona and Jitendra Malik. Scale-space and edge detection using anisotropic diffusion. *PAMI*, 12(7):629–639, 1990.
- Benedek Rozemberczki, Carl Allen, and Rik Sarkar. Multi-scale attributed node embedding. *Journal of Complex Networks*, 9(2):cnab014, 2021.
- T Konstantin Rusch, Benjamin P Chamberlain, James Rowbottom, Siddhartha Mishra, and Michael M Bronstein. Graph-coupled oscillator networks. In *International Conference on Machine Learning*, 2022.
- Michael E Sander, Pierre Ablin, Mathieu Blondel, and Gabriel Peyré. Sinkformers: Transformers with doubly stochastic attention. In *International Conference on Artificial Intelligence and Statistics*, pages 3515–3530. PMLR, 2022.
- Franco Scarselli, Marco Gori, Ah Chung Tsoi, Markus Hagenbuchner, and Gabriele Monfardini. The graph neural network model. *IEEE transactions on neural networks*, 20(1):61–80, 2008.
- Prithviraj Sen, Galileo Namata, Mustafa Bilgic, Lise Getoor, Brian Galligher, and Tina Eliassi-Rad. Collective classification in network data. *AI magazine*, 29(3):93–93, 2008.
- Oleksandr Shchur, Maximilian Mumme, Aleksandar Bojchevski, and Stephan Günnemann. Pitfalls of graph neural network evaluation. In *NIPS workshop*, 2018.
- Alessandro Sperduti. Encoding labeled graphs by labeling raam. *Advances in Neural Information Processing Systems*, 6, 1993.
- Matthew Thorpe, Tan Minh Nguyen, Hedi Xia, Thomas Strohmer, Andrea Bertozzi, Stanley Osher, and Bao Wang. Grand++: Graph neural diffusion with a source term. In *International Conference on Learning Representations*, 2021.
- Jake Topping, Francesco Di Giovanni, Benjamin Paul Chamberlain, Xiaowen Dong, and Michael M Bronstein. Understanding over-squashing and bottlenecks on graphs via curvature. *International Conference on Learning Representations*, 2022.
- Ashish Vaswani, Noam Shazeer, Niki Parmar, Jakob Uszkoreit, Llion Jones, Aidan N Gomez, Łukasz Kaiser, and Illia Polosukhin. Attention is all you need. *Advances in neural information processing systems*, 30, 2017.
- Petar Veličković, Guillem Cucurull, Arantxa Casanova, Adriana Romero, Pietro Liò, and Yoshua Bengio. Graph attention networks. In *International Conference on Learning Representations*, 2018. URL <https://openreview.net/forum?id=rJXmpikCZ>.
- Felix Wu, Amauri Souza, Tianyi Zhang, Christopher Fifty, Tao Yu, and Kilian Weinberger. Simplifying graph convolutional networks. In *International conference on machine learning*, pages 6861–6871. PMLR, 2019. URL <http://proceedings.mlr.press/v97/wu19e.html>.
- Louis-Pascal Xhonneux, Meng Qu, and Jian Tang. Continuous graph neural networks. In *International Conference on Machine Learning*, pages 10432–10441. PMLR, 2020. URL <http://proceedings.mlr.press/v119/xhonneux20a.html>.
- Yujun Yan, Milad Hashemi, Kevin Swersky, Yaoqing Yang, and Danai Koutra. Two sides of the same coin: Heterophily and oversmoothing in graph convolutional neural networks. *arXiv preprint arXiv:2102.06462*, 2021.
- Zhitao Ying, Dylan Bourgeois, Jiaxuan You, Marinka Zitnik, and Jure Leskovec. Gnnexplainer: Generating explanations for graph neural networks. *Advances in neural information processing systems*, 32, 2019.
- Hao Yuan, Haiyang Yu, Shurui Gui, and Shuiwang Ji. Explainability in graph neural networks: A taxonomic survey. *arXiv preprint arXiv:2012.15445*, 2020.

- Lingxiao Zhao and Leman Akoglu. Pairnorm: Tackling oversmoothing in gnns. *arXiv preprint arXiv:1909.12223*, 2019.
- Dengyong Zhou and Bernhard Schölkopf. Regularization on discrete spaces. In *Joint Pattern Recognition Symposium*, pages 361–368. Springer, 2005. URL <https://dennyzhou.github.io/papers/RDS.pdf>.
- Jiong Zhu, Yujun Yan, Lingxiao Zhao, Mark Heimann, Leman Akoglu, and Danai Koutra. Beyond homophily in graph neural networks: Current limitations and effective designs. *Advances in Neural Information Processing Systems*, 33:7793–7804, 2020.

A Proofs and additional details of Section 2

A.1 Discussion on continuous Dirichlet energy and harmonic maps

In this subsection we briefly expand on the formulation of continuous Dirichlet energy in Section 2 to provide more context. Consider a smooth map $f : (M, g) \rightarrow (N, h)$, where N is usually a larger manifold we embed M into, and g, h are Riemannian metrics on domain and codomain respectively. The *Dirichlet energy* of f is defined by

$$\mathcal{E}(f, g, h) := \frac{1}{2} \int_M |df|_g^2 d\mu(g),$$

with $|df|_g$ the norm of the Jacobian of f measured with respect to g and h . If (M, g) is standard Euclidean space \mathbb{R}^n , $N = \mathbb{R}^d$ and h is a constant positive semi-definite matrix, then we can rewrite the Dirichlet energy in a more familiar form as

$$\mathcal{E}(f, h) = \frac{1}{2} \int_{\mathbb{R}^n} \text{trace}(Df^\top h Df) d\mu = \frac{1}{2} \sum_{q,r=1}^d \sum_{j=1}^n \int_{\mathbb{R}^n} h_{qr} \partial_j f^q \partial_j f^r(x) dx.$$

The Dirichlet energy measures the smoothness of the map f , and indeed if h is the identity in \mathbb{R}^d , then we recover the classical definition

$$\mathcal{E}(f) = \frac{1}{2} \sum_{r=1}^d \int_{\mathbb{R}^n} \|\nabla f^r\|^2(x) dx.$$

Gradient flow of Dirichlet energy. Minimizers of \mathcal{E} - referred to as *harmonic maps* - are important objects in geometry: to mention a few, geodesics, minimal isometric immersions and maps $f : M \rightarrow \mathbb{R}^d$ solving $\Delta_g f = 0$ are all instances of harmonic maps. To identify such critical points, one computes the first variation of the energy \mathcal{E} along an arbitrary direction $\partial_t f$, which can be written as

$$d\mathcal{E}_f(\partial_t f) = - \int_M \langle \tau_g(f), \partial_t f \rangle_h d\mu(g).$$

for some tensor field τ with explicit form

$$(\tau_{g_M}(f))^\alpha := \Delta_{g_M} f^\alpha + h_N \Gamma_{\beta\gamma}^\alpha \partial_i f^\beta \partial_j f^\gamma g_M^{ij},$$

for $1 \leq \alpha \leq \dim(N)$, with $\{y^\alpha\}$ local coordinates on N and $\Gamma_{\beta\gamma}^\alpha$ Christoffel symbols. It follows that harmonic maps are identified by the condition $\tau_g(f) = 0$. In [Eells and Sampson \[1964\]](#), the pivotal idea of harmonic map flow – which has shaped much of modern research in geometric analysis – was introduced for the first time: in order to identify minimizers of \mathcal{E} , an input map f_0 is evolved along the direction of (minus) the gradient of the energy \mathcal{E} leading to the dynamics

$$\partial_t f = \tau_g(f). \tag{17}$$

As a special case, when the target space is the classical Euclidean space one recovers the *heat equation* induced by the input Riemannian structure. We also note that when (M, g) is a surface representing an image and $f : (u_1, u_2) \mapsto (u_1, u_2, \phi(u_1, u_2))$ with ϕ a color map, then eq. (17) becomes

$$\partial_t \phi = \text{div}(C_g \nabla \phi), \tag{18}$$

with C_g a constant depending on the metric on M . If we now let g to depend on ϕ , one can recover the celebrated Perona-Malik flow [Kimmel et al. \[1997\]](#).

A.2 Review of Kronecker product and properties of Laplacian kernel

Additional notations and conventions used throughout the appendix. Any graph G is taken to be *connected*. We order the eigenvalues of the graph Laplacian as $0 = \lambda_0^\Delta \leq \lambda_1^\Delta \leq \dots \leq \lambda_{n-1}^\Delta = \rho_\Delta \leq 2$ with associated orthonormal basis of eigenvectors $\{\phi_i^\Delta\}_{i=0}^{n-1}$ so that in particular we have $\Delta \phi_0^\Delta = \mathbf{0}$. Moreover, given a symmetric matrix \mathbf{B} , we generally denote the spectrum of \mathbf{B} by $\text{spec}(\mathbf{B})$. Finally, if we write $\mathbf{F}(t)/\|\mathbf{F}(t)\|$ we always take the norm to be the Frobenius one and tacitly assume that the dynamics is s.t. the solution is not zero.

Kronecker product. In this subsection we summarize a few relevant notions pertaining the Kronecker product of matrices that are going to be applied throughout our spectral analysis of gradient flow equations for GNNs in both the continuous and discrete time setting.

Given a matricial equation of the form

$$\mathbf{Y} = \mathbf{A}\mathbf{X}\mathbf{B},$$

we can vectorize \mathbf{X} and \mathbf{Y} by stacking columns into $\text{vec}(\mathbf{X})$ and $\text{vec}(\mathbf{Y})$ respectively, and rewrite the previous system as

$$\text{vec}(\mathbf{Y}) = (\mathbf{B}^\top \otimes \mathbf{A}) \text{vec}(\mathbf{X}). \quad (19)$$

If \mathbf{A} and \mathbf{B} are symmetric with spectra $\text{spec}(\mathbf{A})$ and $\text{spec}(\mathbf{B})$ respectively, then the spectrum of $\mathbf{B} \otimes \mathbf{A}$ is given by $\text{spec}(\mathbf{A}) \cdot \text{spec}(\mathbf{B})$. Namely, if $\mathbf{A}\mathbf{x} = \lambda^{\mathbf{A}}\mathbf{x}$ and $\mathbf{B}\mathbf{y} = \lambda^{\mathbf{B}}\mathbf{y}$, for \mathbf{x} and \mathbf{y} non-zero vectors, then $\lambda^{\mathbf{B}}\lambda^{\mathbf{A}}$ is an eigenvalue of $\mathbf{B} \otimes \mathbf{A}$ with eigenvector $\mathbf{y} \otimes \mathbf{x}$:

$$(\mathbf{B} \otimes \mathbf{A}) \mathbf{y} \otimes \mathbf{x} = (\lambda^{\mathbf{B}}\lambda^{\mathbf{A}}) \mathbf{y} \otimes \mathbf{x}. \quad (20)$$

One can also define the *Kronecker sum* of matrices $\mathbf{A} \in \mathbb{R}^{n \times n}$ and $\mathbf{B} \in \mathbb{R}^{d \times d}$ as

$$\mathbf{A} \oplus \mathbf{B} := \mathbf{A} \otimes \mathbf{I}_d + \mathbf{I}_n \otimes \mathbf{B}, \quad (21)$$

with spectrum $\text{spec}(\mathbf{A} \oplus \mathbf{B}) = \{\lambda^{\mathbf{A}} + \lambda^{\mathbf{B}} : \lambda^{\mathbf{A}} \in \text{spec}(\mathbf{A}), \lambda^{\mathbf{B}} \in \text{spec}(\mathbf{B})\}$.

Additional details on \mathcal{E}^{Dir} and the choice of Laplacian. We recall that the classical graph Dirichlet energy \mathcal{E}^{Dir} is defined by

$$\mathcal{E}^{\text{Dir}}(\mathbf{F}) = \frac{1}{2} \text{trace}(\mathbf{F}^\top \mathbf{\Delta} \mathbf{F}),$$

where the (unusual) extra factor of $\frac{1}{2}$ is to avoid rescaling the gradient flow by 2 – which is the more common convention. We can use the Kronecker product to rewrite the Dirichlet energy as

$$\mathcal{E}^{\text{Dir}}(\mathbf{F}) = \frac{1}{2} \text{vec}(\mathbf{F})^\top (\mathbf{I}_d \otimes \mathbf{\Delta}) \text{vec}(\mathbf{F}), \quad (22)$$

from which we immediately derive that $\nabla_{\text{vec}(\mathbf{F})} \mathcal{E}^{\text{Dir}}(\mathbf{F}) = (\mathbf{I}_d \otimes \mathbf{\Delta}) \text{vec}(\mathbf{F})$ – since $\mathbf{\Delta}$ is *symmetric* – and hence recover the gradient flow in eq. (3) leading to the graph heat equation across each channel.

Before we further comment on the characterizations of LFD and HFD dynamics, we review the main choices of graph Laplacian and the associated harmonic signals (i.e. how we can characterize the kernel spaces of the given Laplacian operator). Recall that throughout the appendix we always assume that the underlying graph G is *connected*. The symmetrically normalized Laplacian $\mathbf{\Delta} = \mathbf{I} - \mathbf{A}$ is symmetric, positive semi-definite with harmonic space of the form Chung and Graham [1997]

$$\ker(\mathbf{\Delta}) := \text{span}(\mathbf{D}^{\frac{1}{2}} \mathbf{1}_n : \mathbf{1}_n = (1, \dots, 1)^\top). \quad (23)$$

This confirms that if a given GNN evolution $\dot{\mathbf{F}}(t) = \text{GNN}_\theta(\mathbf{F}(t), t)$ with initial condition $\mathbf{F}(0)$ over-smooths as per Definition 2.1 – i.e. $\Delta \mathbf{f}^r(t) \rightarrow \mathbf{0}$ for $t \rightarrow \infty$ for each column $1 \leq r \leq d$ – then the only information persisting in the asymptotic regime is the degree and any dependence on the input features is lost, as studied in Oono and Suzuki [2020], Cai and Wang [2020]. A slightly different behaviour occurs if instead of $\mathbf{\Delta}$, we consider the unnormalized Laplacian $\mathbf{L} = \mathbf{D} - \mathbf{A}$ with kernel $\text{span}(\mathbf{1}_n)$, meaning that if $\mathbf{L}\mathbf{f}^r(t) \rightarrow \mathbf{0}$ as $t \rightarrow \infty$ for each $1 \leq r \leq d$, then any node would be embedded to a single point, hence making any separation task impossible. The same consequence applies to the random walk Laplacian $\mathbf{\Delta}_{\text{RW}} = \mathbf{I} - \mathbf{D}^{-1}\mathbf{A}$. In particular, we note that generally a row-stochastic matrix is not symmetric – if it was, then this would in fact be doubly-stochastic – and the same applies to the random-walk Laplacian (a special exception is given by the class of *regular* graphs). In fact, in general any dynamical system governed by $\mathbf{\Delta}_{\text{RW}}$ (or simply $\mathbf{D}^{-1}\mathbf{A}$) is not the gradient flow of an energy due to the lack of symmetry, as further confirmed below in eq. (25).

A.3 Additional details on LFD and HFD characterizations

In this subsection we provide further details and justifications for Definition 2.1 and Definition 2.2. We first prove the following simple properties.

Lemma A.1. *Assume we have a (continuous) process $t \mapsto \mathbf{F}(t) \in \mathbb{R}^{n \times d}$, for $t \geq 0$. The following equivalent characterizations hold:*

- (i) $\mathcal{E}^{\text{Dir}}(\mathbf{F}(t)) \rightarrow 0$ for $t \rightarrow \infty$ if and only if $\Delta \mathbf{f}^r(t) \rightarrow \mathbf{0}$, for $1 \leq r \leq d$.
- (ii) $\mathcal{E}^{\text{Dir}}(\mathbf{F}(t)/\|\mathbf{F}(t)\|) \rightarrow \rho_\Delta/2$ for $t \rightarrow \infty$ if and only if for any sequence $t_j \rightarrow \infty$ there exist a subsequence $t_{j_k} \rightarrow \infty$ and a unit limit \mathbf{F}_∞ – depending on the subsequence – such that $\Delta \mathbf{f}_\infty^r = \rho_\Delta \mathbf{f}_\infty^r$, for $1 \leq r \leq d$.

Proof. (i) Given $\mathbf{F}(t) \in \mathbb{R}^{n \times d}$, we can vectorize it and decompose it in the orthonormal basis $\{\mathbf{e}_r \otimes \phi_i^\Delta : 1 \leq r \leq d, 0 \leq i \leq n-1\}$, with $\{\mathbf{e}_r\}_{r=1}^d$ canonical basis in \mathbb{R}^d , and write

$$\text{vec}(\mathbf{F}(t)) = \sum_{r,i} c_{r,i}(t) \mathbf{e}_r \otimes \phi_i^\Delta, \quad c_{r,i}(t) := \langle \text{vec}(\mathbf{F}(t)), \mathbf{e}_r \otimes \phi_i^\Delta \rangle.$$

We can then use eq. (22) to compute the Dirichlet energy as

$$\mathcal{E}^{\text{Dir}}(\mathbf{F}(t)) = \frac{1}{2} \sum_{r=1}^d \sum_{i=0}^{n-1} c_{r,i}^2(t) \lambda_i^\Delta \equiv \frac{1}{2} \sum_{r=1}^d \sum_{i=1}^{n-1} c_{r,i}^2(t) \lambda_i^\Delta \geq \frac{1}{2} \text{gap}(\Delta) \sum_{r=1}^d \sum_{i=1}^{n-1} c_{r,i}^2(t),$$

where we have used the convention above that the eigenvector ϕ_0^Δ is in the kernel of Δ . Therefore

$$\mathcal{E}^{\text{Dir}}(\mathbf{F}(t)) \rightarrow 0 \iff \sum_{r=1}^d \sum_{i=1}^{n-1} c_{r,i}^2(t) \rightarrow 0, \quad t \rightarrow \infty,$$

which occurs if and only if

$$(\mathbf{I}_d \otimes \Delta) \text{vec}(\mathbf{F}(t)) = \sum_{r=1}^d \sum_{i=1}^{n-1} c_{r,i}(t) \lambda_i^\Delta \mathbf{e}_r \otimes \phi_i^\Delta \rightarrow 0.$$

(ii) The argument here is similar. Indeed we can write $\mathbf{Q}(t) = \mathbf{F}(t)/\|\mathbf{F}(t)\|$ with $\mathbf{Q}(t)$ a unit-norm signal. Namely, we can vectorize and write

$$\text{vec}(\mathbf{Q}(t)) = \sum_{r,i} q_{r,i}(t) \mathbf{e}_r \otimes \phi_i^\Delta, \quad \sum_{r,i} q_{r,i}^2(t) = 1.$$

Then $\mathcal{E}^{\text{Dir}}(\mathbf{Q}(t)) \rightarrow \rho_\Delta/2$ if and only if

$$\sum_{r,i} q_{r,i}^2(t) \lambda_i^\Delta \rightarrow \rho_\Delta, \quad t \rightarrow \infty,$$

which holds if and only if

$$\begin{aligned} \sum_r q_{r,\rho_\Delta}^2(t) &\rightarrow 1 \\ q_{r,i}^2(t) &\rightarrow 0, \quad i : \lambda_i^\Delta < \rho_\Delta, \end{aligned} \quad (24)$$

given the unit norm constraint. This is equivalent to the Rayleigh quotient of $\mathbf{I}_d \otimes \Delta$ converging to its maximal value ρ_Δ . When this occurs, for any sequence $t_j \rightarrow \infty$ we have that $q_{r,i}^2(t_j) \leq 1$, meaning that we can extract a converging subsequence that due to eq. (24) will converge to a unit eigenvector \mathbf{Q}_∞ of $\mathbf{I}_d \otimes \Delta$ satisfying $(\mathbf{I}_d \otimes \Delta) \mathbf{Q}_\infty = \rho_\Delta \mathbf{Q}_\infty$. Conversely assume for a contradiction that there exists a sequence $t_j \rightarrow \infty$ such that $\mathcal{E}^{\text{Dir}}(\mathbf{F}(t_j)/\|\mathbf{F}(t_j)\|) < \rho_\Delta/2 - \epsilon$, for some $\epsilon > 0$. Then eq. (24) fails to be satisfied along the sequence, meaning that no subsequence converges to a unit norm eigenvector \mathbf{F}_∞ of $\mathbf{I}_d \otimes \Delta$ with associated eigenvalue ρ_Δ which is a contradiction to our assumption. \square

Before we address the formulation of low(high)-frequency-dominated dynamics, we solve explicitly the system $\dot{\mathbf{F}}(t) = \mathbf{A} \mathbf{F}(t)$ in $\mathbb{R}^{n \times d}$, with some initial condition $\mathbf{F}(0)$. We can vectorize the equation and solve $\text{vec}(\dot{\mathbf{F}}(t)) = (\mathbf{I}_d \otimes \mathbf{A}) \text{vec}(\mathbf{F}(t))$, meaning that

$$\text{vec}(\mathbf{F}(t)) = \sum_{r=1}^d \sum_{i=0}^{n-1} e^{(1-\lambda_i^\Delta)t} c_{r,i}(0) \mathbf{e}_r \otimes \phi_i^\Delta, \quad c_{r,i}(0) := \langle \text{vec}(\mathbf{F}(0)), \mathbf{e}_r \otimes \phi_i^\Delta \rangle.$$

Consider any initial condition $\mathbf{F}(0)$ such that

$$\sum_{r=1}^d |c_{r,0}| = \sum_{r=1}^d \left| \langle \text{vec}(\mathbf{F}(0)), \mathbf{e}_r \otimes \phi_0^\Delta \rangle \right| > 0,$$

which is satisfied for each $\text{vec}(\mathbf{F}(0)) \in \mathbb{R}^{nd} \setminus \mathcal{U}^\perp$, where \mathcal{U}^\perp is the orthogonal complement of $\mathbb{R}^d \otimes \text{span}(\phi_0^\Delta)$. Since \mathcal{U}^\perp is a lower-dimensional subspace, its complement is dense. Accordingly for a.e. $\mathbf{F}(0)$, we find that the solution satisfies

$$\|\text{vec}(\mathbf{F}(t))\|^2 = e^{2t} \left(\sum_{r=1}^d c_{r,0}^2 + \mathcal{O}(e^{-2\text{gap}(\Delta)t}) \right) = e^{2t} \left(\|P_{\ker(\Delta)}^\perp \text{vec}(\mathbf{F}(0))\|^2 + \mathcal{O}(e^{-2\text{gap}(\Delta)t}) \right),$$

with $P_{\ker(\Delta)}^\perp$ the projection onto $\mathbb{R}^d \otimes \ker(\Delta)$. We see that the norm of the solution increases exponentially, however *the dominant term is given by the projection onto the lowest frequency signal* and in fact

$$\frac{\text{vec}(\mathbf{F}(t))}{\|\text{vec}(\mathbf{F}(t))\|} = \frac{P_{\ker(\Delta)}^\perp \text{vec}(\mathbf{F}(0)) + \mathcal{O}(e^{-\text{gap}(\Delta)t})(\mathbf{I} - P_{\ker(\Delta)}^\perp) \text{vec}(\mathbf{F}(0))}{\left(\|P_{\ker(\Delta)}^\perp \text{vec}(\mathbf{F}(0))\|^2 + \mathcal{O}(e^{-2\text{gap}(\Delta)t}) \right)^{\frac{1}{2}}} \rightarrow \text{vec}(\mathbf{F}_\infty),$$

such that $(\mathbf{I}_d \otimes \Delta) \text{vec}(\mathbf{F}_\infty) = \mathbf{0}$ which means $\Delta \mathbf{f}_\infty^r = \mathbf{0}$, for each column $1 \leq r \leq d$. Equivalently, one can compute $\mathcal{E}^{\text{Dir}}(\mathbf{F}(t)/\|\mathbf{F}(t)\|)$ and conclude that the latter quantity converges to zero as $t \rightarrow \infty$ by the very same argument.

In fact, this motivates further the nomenclature LFD and HFD. Without loss of generality we focus now on the high-frequency case. Assume that we have a HFD dynamics $t \mapsto \mathbf{F}(t)$, i.e. $\mathcal{E}^{\text{Dir}}(\mathbf{F}(t)/\|\mathbf{F}(t)\|) \rightarrow \rho_\Delta/2$, then we can vectorize the solution and write $\text{vec}(\mathbf{F}(t)) = \|\mathbf{F}(t)\| \text{vec}(\mathbf{Q}(t))$, for some time-dependent unit vector $\text{vec}(\mathbf{Q}(t)) \in \mathbb{R}^{nd}$:

$$\text{vec}(\mathbf{Q}(t)) = \sum_{r,i} q_{r,i}(t) \mathbf{e}_r \otimes \phi_i^\Delta, \quad \sum_{r,i} q_{r,i}^2(t) = 1.$$

By Lemma A.1 and more explicitly eq. (24), we derive that the coefficients $\{q_{r,\rho_\Delta}\}$ associated with the eigenvectors $\mathbf{e}_r \otimes \phi_{\rho_\Delta}^\Delta$ are dominant in the evolution hence justifying the name *high-frequency dominated* dynamics.

We note that the next result covers Lemma 2.3.

Lemma A.2. Consider a dynamical system $\dot{\mathbf{F}}(t) = \text{GNN}_\theta(\mathbf{F}(t), t)$, with initial condition $\mathbf{F}(0)$.

- (i) GNN_θ is LFD if and only if $(\mathbf{I}_d \otimes \Delta) \frac{\text{vec}(\mathbf{F}(t))}{\|\mathbf{F}(t)\|} \rightarrow \mathbf{0}$ if and only if for each sequence $t_j \rightarrow \infty$ there exist a subsequence $t_{j_k} \rightarrow \infty$ and \mathbf{F}_∞ (depending on the subsequence) s.t. $\frac{\mathbf{F}(t_{j_k})}{\|\mathbf{F}(t_{j_k})\|} \rightarrow \mathbf{F}_\infty$ satisfying $\Delta \mathbf{f}_\infty^r = \mathbf{0}$, for each $1 \leq r \leq d$.
- (ii) GNN_θ is HFD if and only if for each sequence $t_j \rightarrow \infty$ there exist a subsequence $t_{j_k} \rightarrow \infty$ and \mathbf{F}_∞ (depending on the subsequence) s.t. $\frac{\mathbf{F}(t_{j_k})}{\|\mathbf{F}(t_{j_k})\|} \rightarrow \mathbf{F}_\infty$ satisfying $\Delta \mathbf{f}_\infty^r = \rho_\Delta \mathbf{f}_\infty^r$, for each $1 \leq r \leq d$.

Proof. (i) Since $\Delta \mathbf{f}^r(t) \rightarrow \mathbf{0}$ for each $1 \leq r \leq d$ if and only if $(\mathbf{I}_d \otimes \Delta) \text{vec}(\mathbf{F}(t)) \rightarrow \mathbf{0}$, we conclude that the dynamics is LFD if and only if $(\mathbf{I}_d \otimes \Delta) \frac{\text{vec}(\mathbf{F}(t))}{\|\mathbf{F}(t)\|} \rightarrow \mathbf{0}$ due to (i) in Lemma A.1. Consider a sequence $t_j \rightarrow \infty$. Since $\text{vec}(\mathbf{F}(t_j))/\|\mathbf{F}(t_j)\|$ is a bounded sequence we can extract a converging subsequence t_{j_k} : $\text{vec}(\mathbf{F}(t_{j_k}))/\|\mathbf{F}(t_{j_k})\| \rightarrow \text{vec}(\mathbf{F}_\infty)$. If the dynamics is LFD, then $(\mathbf{I}_d \otimes \Delta) \frac{\text{vec}(\mathbf{F}(t_{j_k}))}{\|\mathbf{F}(t_{j_k})\|} \rightarrow \mathbf{0}$ and hence we conclude that $\text{vec}(\mathbf{F}_\infty) \in \ker(\mathbf{I}_d \otimes \Delta)$. Conversely, assume that for any sequence $t_j \rightarrow \infty$ there exists a subsequence t_{j_k} and \mathbf{F}_∞ such that $\frac{\mathbf{F}(t_{j_k})}{\|\mathbf{F}(t_{j_k})\|} \rightarrow \mathbf{F}_\infty$ satisfying $\Delta \mathbf{f}_\infty^r = \mathbf{0}$, for each $1 \leq r \leq d$. If for a contradiction we had $\varepsilon > 0$ and $t_j \rightarrow \infty$ such that $\mathcal{E}^{\text{Dir}}(\mathbf{F}(t_j)/\|\mathbf{F}(t_j)\|) \geq \varepsilon$ – for j large enough – then by (i) in Lemma A.1 there exist $1 \leq r \leq d$, $i > 0$ and a subsequence t_{j_k} satisfying

$$\left| \left\langle \left(\frac{\text{vec}(\mathbf{F}(t_{j_k}))}{\|\mathbf{F}(t_{j_k})\|} \right), \mathbf{e}_r \otimes \phi_i^\Delta \right\rangle \right| > \delta(\varepsilon) > 0,$$

meaning that there is no subsequence of $\{t_{j_k}\}$ s.t. $(\mathbf{I}_d \otimes \Delta)\text{vec}(\mathbf{F}(t_{j_k}))/\|\mathbf{F}(t_{j_k})\| \rightarrow \mathbf{0}$, providing a contradiction.

(ii) This is equivalent to (ii) in Lemma A.1.

□

Remark. We note that in Lemma 2.3 an LFD dynamics does not necessarily mean that the normalized solution converges to the kernel of $\mathbf{I}_d \otimes \Delta$ – i.e. one in general has always to pass to subsequences. Indeed, we can consider the simple example $t \mapsto \text{vec}(\mathbf{F}(t)) := \cos(t)\mathbf{e}_{\bar{r}} \otimes \phi_0^\Delta$, for some $1 \leq \bar{r} \leq d$, which satisfies $\Delta \mathbf{f}^r(t) = \mathbf{0}$ for each r , but it is not a convergent function due to its oscillatory nature. Same argument applies to HFD.

A.4 Details and proofs on $\mathcal{E}_{\mathbf{W}}^{\text{Dir}}$ and its gradient flow

By direct computation one verifies that the definition in eq. (4) can be equivalently written as

$$\mathcal{E}_{\mathbf{W}}^{\text{Dir}}(\mathbf{F}) = \frac{1}{2} \langle \text{vec}(\mathbf{F}), (\mathbf{W}^\top \mathbf{W} \otimes \Delta) \text{vec}(\mathbf{F}) \rangle,$$

from which we immediately derive $\nabla_{\text{vec}(\mathbf{F})} \mathcal{E}_{\mathbf{W}}^{\text{Dir}}(\text{vec}(\mathbf{F})) = (\mathbf{W}^\top \mathbf{W} \otimes \Delta) \text{vec}(\mathbf{F})$ which proves eq. (5). We can now address the proof of Proposition 2.4.

Proof of Proposition 2.4. We can vectorize the gradient flow system in eq. (5) and use the spectral characterization of $\mathbf{W}^\top \mathbf{W} \otimes \Delta$ in eq. (20) to write the solution explicitly as

$$\text{vec}(\mathbf{F}(t)) = \sum_{r,i} e^{-(\lambda_r^{\mathbf{W}} \lambda_i^\Delta) t} c_{r,i}(0) \phi_r^{\mathbf{W}} \otimes \phi_i^\Delta,$$

where $\{\lambda_r^{\mathbf{W}}\}_r = \text{spec}(\mathbf{W}^\top \mathbf{W}) \subset \mathbb{R}_{\geq 0}$ with associated basis of orthonormal eigenvectors given by $\{\phi_r^{\mathbf{W}}\}_r$. Then

$$\begin{aligned} \mathcal{E}^{\text{Dir}}(\mathbf{F}(t)) &= \frac{1}{2} \langle \text{vec}(\mathbf{F}(t)), (\mathbf{I}_d \otimes \Delta) \text{vec}(\mathbf{F}(t)) \rangle = \frac{1}{2} \sum_{r,i} e^{-2t(\lambda_r^{\mathbf{W}} \lambda_i^\Delta)} c_{r,i}^2(0) \lambda_i^\Delta \\ &= \frac{1}{2} \sum_{r:\lambda_r^{\mathbf{W}}=0,i} c_{r,i}^2(0) \lambda_i^\Delta + \frac{1}{2} \sum_{r:\lambda_r^{\mathbf{W}}>0,i>0} c_{r,i}^2(0) e^{-2t(\lambda_r^{\mathbf{W}} \lambda_i^\Delta)} \lambda_i^\Delta \\ &= \mathcal{E}^{\text{Dir}}((P_{\mathbf{W}}^{\text{ker}} \otimes \mathbf{I}_n) \text{vec}(\mathbf{F}(0))) + \frac{1}{2} \sum_{r:\lambda_r^{\mathbf{W}}>0,i>0} c_{r,i}^2(0) e^{-2t(\lambda_r^{\mathbf{W}} \lambda_i^\Delta)} \lambda_i^\Delta \\ &\leq \mathcal{E}^{\text{Dir}}((P_{\mathbf{W}}^{\text{ker}} \otimes \mathbf{I}_n) \text{vec}(\mathbf{F}(0))) + \frac{\rho_\Delta}{2} e^{-2t \text{gap}(\mathbf{W}^\top \mathbf{W}) \text{gap}(\Delta)} \|\mathbf{F}(0)\|^2, \end{aligned}$$

where we recall that $P_{\mathbf{W}}^{\text{ker}}$ is the projection onto $\ker(\mathbf{W}^\top \mathbf{W})$ and that by convention the index $i = 0$ is associated with the lowest graph frequency $\lambda_0^\Delta = 0$ – by assumption G is connected. This proves that the dynamics is in fact smoothing as per Definition 2.1. By the very same argument we find that

$$\text{vec}(\mathbf{F}(t)) \rightarrow (\mathbf{I}_d \otimes P_{\Delta}^{\text{ker}}) \text{vec}(\mathbf{F}(0)) + (P_{\mathbf{W}}^{\text{ker}} \otimes \mathbf{I}_n) \text{vec}(\mathbf{F}(0)), \quad t \rightarrow \infty,$$

with P_{Δ}^{ker} the orthogonal projection onto $\ker \Delta$ – the other terms decay exponentially to zero. We first focus on the first quantity, which we can write as

$$(\mathbf{I}_d \otimes P_{\Delta}^{\text{ker}}) \text{vec}(\mathbf{F}(0)) = \sum_r c_{r,0}(0) \phi_r^{\mathbf{W}} \otimes \phi_0^\Delta,$$

which has matrix representation $\phi_0^\Delta \phi_\infty^\top \in \mathbb{R}^{n \times d}$ with

$$\phi_\infty := \sum_r c_{r,0}(0) \phi_r^{\mathbf{W}}.$$

By eq. (23) we deduce that the i -th row of $\phi_0^\Delta \phi_\infty^\top \in \mathbb{R}^{n \times d}$ is the d -dimensional vector $\sqrt{d_i} \phi_\infty$. We now focus on the term

$$(P_{\mathbf{W}}^{\text{ker}} \otimes \mathbf{I}_n) \text{vec}(\mathbf{F}(0)) = \sum_{r:\lambda_r^{\mathbf{W}}=0,j} c_{r,j}(0) \phi_r^{\mathbf{W}} \otimes \phi_j^\Delta$$

which has matrix representation $\sum_{r:\lambda_r^{\mathbf{W}}=0,j} c_{r,j}(0)\phi_j^\Delta(\phi_r^{\mathbf{W}})^\top$. In particular, the i -th row is given by

$$\sum_{r:\lambda_r^{\mathbf{W}}=0,j} c_{r,j}(0)(\phi_j^\Delta)_i\phi_r^{\mathbf{W}} = P_{\mathbf{W}}^{\ker} \mathbf{f}_i(0).$$

This completes the proof of Proposition 2.4. \square

B Proofs and additional details of Section 3

B.1 Spectral analysis of the channel-mixing: the continuous case

Consider the generalized energy \mathcal{E}^{tot} in eq. (7). We can use vectorization to rewrite it as

$$\mathcal{E}^{\text{tot}}(\text{vec}(\mathbf{F})) = \frac{1}{2}\langle \text{vec}(\mathbf{F}), (\boldsymbol{\Omega} \otimes \mathbf{I}_n)\text{vec}(\mathbf{F}) \rangle - \frac{1}{2}\langle \text{vec}(\mathbf{F}), (\mathbf{W} \otimes \bar{\mathbf{A}})\text{vec}(\mathbf{F}) \rangle,$$

from which the gradient flow in eq. (8) follows. In particular, given a system as in eq. (8):

$$\text{vec}(\dot{\mathbf{F}}(t)) = -(\boldsymbol{\Omega} \otimes \mathbf{I}_n)\text{vec}(\mathbf{F}(t)) + (\mathbf{W} \otimes \bar{\mathbf{A}})\text{vec}(\mathbf{F}(t)),$$

if this is the gradient flow of $\mathbf{F} \mapsto \mathcal{E}^{\text{tot}}(\mathbf{F})$, then we would have

$$\nabla_{\text{vec}(\mathbf{F})}^2 \mathcal{E}^{\text{tot}}(\mathbf{F}) = \boldsymbol{\Omega} \otimes \mathbf{I}_n - \mathbf{W} \otimes \bar{\mathbf{A}}, \quad (25)$$

which must be symmetric due to the Hessian of a function being symmetric. The latter means

$$(\boldsymbol{\Omega}^\top - \boldsymbol{\Omega}) \otimes \mathbf{I}_n = (\mathbf{W}^\top - \mathbf{W}) \otimes \bar{\mathbf{A}},$$

which is satisfied if and only if both $\boldsymbol{\Omega}$ and \mathbf{W} are *symmetric*. This shows that eq. (8) is the gradient flow of \mathcal{E}^{tot} if and only if $\boldsymbol{\Omega}$ and \mathbf{W} are symmetric.

We now rely on the spectral decomposition of \mathbf{W} to rewrite \mathcal{E}^{tot} explicitly in terms of attractive and repulsive interactions. If we have a spectral decomposition $\mathbf{W} = \mathbf{U}\boldsymbol{\Lambda}\mathbf{U}^\top$, we can separate the positive eigenvalues from the negative ones and write

$$\mathbf{W} = \mathbf{U}\boldsymbol{\Lambda}_+\mathbf{U}^\top + \mathbf{U}\boldsymbol{\Lambda}_-\mathbf{U}^\top := \mathbf{W}_+ - \mathbf{W}_-.$$

Since $\mathbf{W}_+ \succcurlyeq 0, \mathbf{W}_- \preccurlyeq 0$, we can use the Choleski decomposition to write $\mathbf{W}_+ = \boldsymbol{\Theta}_+^\top \boldsymbol{\Theta}_+$ and $\mathbf{W}_- = \boldsymbol{\Theta}_-^\top \boldsymbol{\Theta}_-$ with $\boldsymbol{\Theta}_+, \boldsymbol{\Theta}_- \in \mathbb{R}^{d \times d}$. Equation (9) follows then by direct computation: namely

$$\begin{aligned} \mathcal{E}^{\text{tot}}(\mathbf{F}) &= \frac{1}{2} \sum_i \langle \mathbf{f}_i, \boldsymbol{\Omega} \mathbf{f}_i \rangle - \frac{1}{2} \sum_{i,j} \bar{a}_{ij} \langle \mathbf{f}_i, \mathbf{W} \mathbf{f}_j \rangle \\ &= \frac{1}{2} \sum_i \langle \mathbf{f}_i, (\boldsymbol{\Omega} - \mathbf{W}) \mathbf{f}_i \rangle + \frac{1}{2} \sum_i \langle \mathbf{f}_i, \mathbf{W} \mathbf{f}_i \rangle - \frac{1}{2} \sum_{i,j} \bar{a}_{ij} \langle \boldsymbol{\Theta}_+ \mathbf{f}_i, \boldsymbol{\Theta}_+ \mathbf{f}_j \rangle + \frac{1}{2} \sum_{i,j} \bar{a}_{ij} \langle \boldsymbol{\Theta}_- \mathbf{f}_i, \boldsymbol{\Theta}_- \mathbf{f}_j \rangle \\ &= \frac{1}{2} \sum_i \langle \mathbf{f}_i, (\boldsymbol{\Omega} - \mathbf{W}) \mathbf{f}_i \rangle + \frac{1}{4} \sum_{i,j} \|\boldsymbol{\Theta}_+ (\nabla \mathbf{F})_{ij}\|^2 - \frac{1}{4} \sum_{i,j} \|\boldsymbol{\Theta}_- (\nabla \mathbf{F})_{ij}\|^2, \end{aligned}$$

where we have used that $\sum_{i,j} \frac{1}{d_i} \|\boldsymbol{\Theta}_+ \mathbf{f}_i\|^2 = \sum_i \|\boldsymbol{\Theta}_+ \mathbf{f}_i\|^2$.

Proof of Proposition 3.1. Once we compute the spectrum of $\mathbf{W} \otimes \bar{\mathbf{A}}$ via eq. (20), we can write the solution as – recall that $\bar{\mathbf{A}} = \mathbf{I}_n - \boldsymbol{\Delta}$ so we can rephrase the eigenvalues of $\bar{\mathbf{A}}$ in terms of the eigenvalues of $\boldsymbol{\Delta}$:

$$\text{vec}(\mathbf{F}(t)) = \sum_{r,i} e^{\lambda_r^{\mathbf{W}}(1-\lambda_i^\Delta)t} c_{r,i}(0) \phi_r^{\mathbf{W}} \otimes \phi_i^\Delta,$$

with $\mathbf{W} \phi_r^{\mathbf{W}} = \lambda_r^{\mathbf{W}} \phi_r^{\mathbf{W}}$, for $1 \leq r \leq d$, where $\{\phi_r^{\mathbf{W}}\}_r$ is an orthonormal basis of eigenvectors in \mathbb{R}^d . We can then calculate the Dirichlet energy along the solution as

$$\mathcal{E}^{\text{Dir}}(\mathbf{F}(t)) = \frac{1}{2} \langle \text{vec}(\mathbf{F}(t)), (\mathbf{I}_d \otimes \boldsymbol{\Delta}) \text{vec}(\mathbf{F}(t)) \rangle = \frac{1}{2} \sum_{r,i} e^{2\lambda_r^{\mathbf{W}}(1-\lambda_i^\Delta)t} c_{r,i}^2(0) \lambda_i^\Delta.$$

We now consider two cases:

- If $\lambda_r^{\mathbf{W}} > 0$, then $\lambda_r^{\mathbf{W}}(1 - \lambda_i^{\Delta}) \leq \lambda_+^{\mathbf{W}}$.
- If $\lambda_r^{\mathbf{W}} < 0$, then $\lambda_r^{\mathbf{W}}(1 - \lambda_i^{\Delta}) \leq |\lambda_-^{\mathbf{W}}|(\rho_{\Delta} - 1) := \rho_-$, with eigenvectors $\phi_r^{\mathbf{W}} \otimes \phi_{\rho_{\Delta}}^{\Delta}$ for each r s.t. $\mathbf{W}\phi_r^{\mathbf{W}} = \lambda_r^{\mathbf{W}}\phi_r^{\mathbf{W}}$ – without loss of generality we can assume that ρ_{Δ} is a simple eigenvalue for Δ . In particular, if $\lambda_r^{\mathbf{W}} < 0$ and $\lambda_r^{\mathbf{W}}(1 - \lambda_i^{\Delta}) < \rho_-$, then

$$\lambda_r^{\mathbf{W}}(1 - \lambda_i^{\Delta}) < \max\{|\lambda_-^{\mathbf{W}}|(\lambda_{n-2}^{\Delta} - 1), |\lambda_{-,2}^{\mathbf{W}}|(\rho_{\Delta} - 1)\},$$

where $\lambda_{-,2}^{\mathbf{W}}$ is the second most negative eigenvalue of \mathbf{W} and λ_{n-2}^{Δ} is the second largest eigenvalue of Δ . In particular, we can write

$$\lambda_{n-2}^{\Delta} = \rho_{\Delta} - \text{gap}(\rho_{\Delta}\mathbf{I}_n - \Delta), \quad |\lambda_{-,2}^{\mathbf{W}}| = |\lambda_-^{\mathbf{W}}| - \text{gap}(|\lambda_-^{\mathbf{W}}|\mathbf{I}_d + \mathbf{W}). \quad (26)$$

From (i) and (ii) we derive that if $\lambda_r^{\mathbf{W}}(1 - \lambda_i^{\Delta}) \neq \rho_-$, then

$$\begin{aligned} \lambda_r^{\mathbf{W}}(1 - \lambda_i^{\Delta}) - \rho_- &< -\min\{\rho_- - \lambda_+^{\mathbf{W}}, \rho_- - |\lambda_-^{\mathbf{W}}|(\lambda_{n-2}^{\Delta} - 1), \rho_- - |\lambda_{-,2}^{\mathbf{W}}|(\rho_{\Delta} - 1)\} \\ &= -\min\{\rho_- - \lambda_+^{\mathbf{W}}, |\lambda_-^{\mathbf{W}}|\text{gap}(\rho_{\Delta}\mathbf{I} - \Delta), \text{gap}(|\lambda_-^{\mathbf{W}}|\mathbf{I} + \mathbf{W})(\rho_{\Delta} - 1)\} = -\epsilon_{\text{HFD}}, \end{aligned}$$

where we have used eq. (26). Accordingly, if $\rho_- > \lambda_+^{\mathbf{W}}$, then

$$\begin{aligned} \mathcal{E}^{\text{Dir}}(\mathbf{F}(t)) &= e^{2t\rho_-} \left(\frac{\rho_{\Delta}}{2} \sum_{r:\lambda_r^{\mathbf{W}}=\lambda_-^{\mathbf{W}}} c_{r,\rho_{\Delta}}^2(0) + \frac{1}{2} \sum_{r,i:\lambda_r^{\mathbf{W}}(1-\lambda_i^{\Delta})\neq\rho_-} e^{2(\lambda_r^{\mathbf{W}}(1-\lambda_i^{\Delta})-\rho_-)t} c_{r,i}^2(0) \right) \\ &= e^{2t\rho_-} \left(\frac{\rho_{\Delta}}{2} \|P_{\mathbf{W}}^{\rho_-} \mathbf{F}(0)\|^2 + \mathcal{O}(e^{-2t\epsilon_{\text{HFD}}}) \right). \end{aligned}$$

By the same argument we can factor out the dominant term and derive the following limit for $t \rightarrow \infty$ and for a.e. $\mathbf{F}(0)$ since $P_{\mathbf{W}}^{\rho_-} \text{vec}(\mathbf{F}(0)) = \mathbf{0}$ only if $\text{vec}(\mathbf{F}(0))$ belongs to a lower dimensional subspace of \mathbb{R}^{nd} :

$$\frac{\text{vec}(\mathbf{F}(t))}{\text{vec}(\mathbf{F}(0))} = \frac{P_{\mathbf{W}}^{\rho_-} \text{vec}(\mathbf{F}(0)) + \mathcal{O}(e^{-\epsilon_{\text{HFD}}t})((\mathbf{I} - P_{\mathbf{W}}^{\rho_-})\text{vec}(\mathbf{F}(0)))}{(\|P_{\mathbf{W}}^{\rho_-} \text{vec}(\mathbf{F}(0))\|^2 + \mathcal{O}(e^{-2\epsilon_{\text{HFD}}t}))^{\frac{1}{2}}} \rightarrow \frac{P_{\mathbf{W}}^{\rho_-} \text{vec}(\mathbf{F}(0))}{\|P_{\mathbf{W}}^{\rho_-} \text{vec}(\mathbf{F}(0))\|},$$

where the latter is a unit vector $\text{vec}(\mathbf{F}_{\infty})$ satisfying $(\mathbf{I}_d \otimes \Delta)\text{vec}(\mathbf{F}_{\infty}) = \rho_{\Delta}\text{vec}(\mathbf{F}_{\infty})$, which completes the proof. \square

B.2 Propagating with $-\Delta$: a perspective in terms of channel-mixing spectrum

In this subsection we briefly review the special case of eq. (8) where $\Omega = \mathbf{W}$, and comment on why we generally expect a framework where the propagation is governed by the graph vector field $\bar{\mathbf{A}}$ to be more flexible than one with $-\Delta$. If $\Omega = \mathbf{W}$, the gradient flow in eq. (8) becomes

$$\dot{\mathbf{F}}(t) = -\Delta\mathbf{F}(t)\mathbf{W}. \quad (27)$$

We note that once vectorized, the solution to the dynamical system can be written as

$$\text{vec}(\mathbf{F}(t)) = \sum_{r=1}^d \sum_{i=0}^{n-1} e^{-\lambda_r^{\mathbf{W}}\lambda_i^{\Delta}t} c_{r,i}(0) \phi_r^{\mathbf{W}} \otimes \phi_i^{\Delta}.$$

In particular, we immediately deduce the following counterpart to Proposition 3.1

Corollary B.1. *If $\text{spec}(\mathbf{W}) \cap \mathbb{R}_- \neq \emptyset$, then eq. (27) is HFD for a.e. $\mathbf{F}(0)$.*

Differently from eq. (8) the lowest frequency component is *always preserved independent of the spectrum of \mathbf{W}* . This means that the system cannot learn eigenvalues of \mathbf{W} to either magnify or suppress the low-frequency projection. In contrast, this can be done if $\Omega = \mathbf{0}$, or equivalently one replaces $-\Delta$ with $\bar{\mathbf{A}}$ providing a further justification in terms of the interaction between graph spectrum and channel-mixing spectrum for why graph convolutional models use the normalized adjacency rather than the Laplacian for propagating messages Kipf and Welling [2017].

B.3 A more general family of energies: gradient flow with non-linear activations

Consider a more general pairwise energy including a non-linear differentiable activation map σ of the form

$$\mathcal{E}_{\sigma, \mathbf{W}}^{\text{pair}}(\mathbf{F}) = \frac{1}{2} \sum_{i,j} \bar{a}_{i,j} \sigma(\mathbf{f}_i, \mathbf{W}\mathbf{f}_j).$$

We temporarily assume that $\Omega = \mathbf{0}$. The gradient flow follows from direct computation:

$$\dot{\mathbf{F}}(t) = \mathcal{A}_{\sigma}(\mathbf{F}(t))\mathbf{F}(t)\mathbf{W}, \quad (\mathcal{A}_{\sigma}(\mathbf{F}(t)))_{ij} := \bar{a}_{ij}\sigma'(\mathbf{f}_i, \mathbf{W}\mathbf{f}_j). \quad (28)$$

In particular, we see that the non-linear activations in general may induce a type of attention mechanism where the diffusion along edges is controlled by the derivative of σ evaluated on the inner product of features induced by \mathbf{W} . A similar structure is investigated in [Eliasof et al. \[2021\]](#). We also observe that analogous conclusions can be deduced if $\Omega \neq \mathbf{0}$ and the external energy term $\mathcal{E}_{\Omega}^{\text{ext}}$ includes a non-linear activation map σ as in the pairwise contribution.

C Proofs and additional details of Section 4

C.1 Comparison with continuous GNNs: details and proofs

We prove the following result which covers [Proposition 4.1](#).

Proof of Proposition 4.1. We structure the proof by following the numeration in the statement.

(i) From direct computation we find

$$\begin{aligned} \frac{d\mathcal{E}^{\text{Dir}}(\mathbf{F}(t))}{dt} &= \frac{1}{2} \frac{d}{dt} (\langle \text{vec}(\mathbf{F}(t)), (\mathbf{I}_d \otimes \Delta) \text{vec}(\mathbf{F}(t)) \rangle) \\ &= -\langle \text{vec}(\mathbf{F}(t)), (\mathbf{K}^{\top}(t)\mathbf{K}(t) \otimes \Delta^2) \text{vec}(\mathbf{F}(t)) \rangle \leq 0, \end{aligned}$$

since $\mathbf{K}^{\top}(t)\mathbf{K}(t) \otimes \Delta^2 \succeq 0$. Note that we have used that $(\mathbf{A} \otimes \mathbf{B})(\mathbf{C} \otimes \mathbf{D}) = \mathbf{AC} \otimes \mathbf{BD}$.

(ii) We consider the dynamical system

$$\dot{\mathbf{F}}_{\text{CGNN}}(t) = -\Delta\mathbf{F}(t) + \mathbf{F}(t)\tilde{\Omega} + \mathbf{F}(0).$$

We can write $\text{vec}(\mathbf{F}(t)) = \sum_{r,i} c_{r,i}(t) \phi_r^{\tilde{\Omega}} \otimes \phi_i^{\Delta}$, leading to the system

$$\dot{c}_{r,i}(t) = (\lambda_r^{\tilde{\Omega}} - \lambda_i^{\Delta})c_{r,i}(t) + c_{r,i}(0), \quad 0 \leq i \leq n-1, \quad 1 \leq r \leq d.$$

We can solve explicitly the system as

$$\begin{aligned} c_{r,i}(t) &= c_{r,i}(0) \left(e^{(\lambda_r^{\tilde{\Omega}} - \lambda_i^{\Delta})t} \left(1 + \frac{1}{\lambda_r^{\tilde{\Omega}} - \lambda_i^{\Delta}} \right) - \frac{1}{\lambda_r^{\tilde{\Omega}} - \lambda_i^{\Delta}} \right), \quad \text{if } \lambda_r^{\tilde{\Omega}} \neq \lambda_i^{\Delta} \\ c_{r,i}(t) &= c_{r,i}(0)(1+t), \quad \text{otherwise.} \end{aligned}$$

We see now that for a.e. $\mathbf{F}(0)$ the projection $(\mathbf{I}_d \otimes \phi_{\rho_{\Delta}}^{\Delta} (\phi_{\rho_{\Delta}}^{\Delta})^{\top}) \text{vec}(\mathbf{F}(t))$ is never the dominant term. In fact, if there exists r s.t. $\lambda_r^{\tilde{\Omega}} \geq \rho_{\Delta}$, then $\lambda_r^{\tilde{\Omega}} - \lambda_i^{\Delta} > \lambda_r^{\tilde{\Omega}} - \rho_{\Delta}$, for any other non-maximal graph Laplacian eigenvalue. It follows that there is *no* $\tilde{\Omega}$ s.t. the normalized solution maximizes the Rayleigh quotient of $\mathbf{I}_d \otimes \Delta$, proving that CGNN is never HFD.

If we have no source, then the CGNN equation becomes

$$\dot{\mathbf{F}}(t) = -\Delta\mathbf{F}(t) + \mathbf{F}(t)\tilde{\Omega} \iff \text{vec}(\dot{\mathbf{F}}(t)) = (\tilde{\Omega} \oplus (-\Delta))\text{vec}(\mathbf{F}(t)),$$

using the Kronecker sum notation in eq. [\(21\)](#). It follows that we can write the vectorized solution in the basis $\{\phi_r^{\tilde{\Omega}} \otimes \phi_i^{\Delta}\}_{r,i}$ as

$$\begin{aligned} \text{vec}(\mathbf{F}(t)) &= e^{\lambda_+^{\tilde{\Omega}} t} \left(\sum_{r:\lambda_r^{\tilde{\Omega}} = \lambda_+^{\tilde{\Omega}}} c_{r,0}(0) \phi_r^{\tilde{\Omega}} \otimes \phi_0^{\Delta} + \mathcal{O}(e^{-\text{gap}(\lambda_+^{\tilde{\Omega}} \mathbf{I}_d - \tilde{\Omega})t}) \sum_{r:\lambda_r^{\tilde{\Omega}} < \lambda_+^{\tilde{\Omega}}} c_{r,0}(0) \phi_r^{\tilde{\Omega}} \otimes \phi_0^{\Delta} \right) \\ &\quad + e^{\lambda_+^{\tilde{\Omega}} t} \left(\mathcal{O}(e^{-\text{gap}(\Delta)t}) \left(\sum_{r,i>0} c_{r,i}(0) \phi_r^{\tilde{\Omega}} \otimes \phi_i^{\Delta} \right) \right), \end{aligned}$$

meaning that the dominant term is given by the lowest frequency component and in fact, if we normalize we find $\mathcal{E}^{\text{Dir}}(\mathbf{F}(t)/\|\mathbf{F}(t)\|) \leq e^{-\text{gap}(\Delta)t}$.

(iii) Finally we consider the dynamical system induced by linear GRAND

$$\dot{\mathbf{F}}_{\text{GRAND}}(t) = -\Delta_{\text{RW}}\mathbf{F}(t) = -(\mathbf{I} - \mathcal{A}(\mathbf{F}(0)))\mathbf{F}(t).$$

Since we have no channel-mixing, without loss of generality we can assume that $d = 1$ – one can then extend the argument to any entry. We can use the Jordan form of \mathcal{A} to write the solution of the GRAND dynamical system as

$$\mathbf{f}(t) = P \text{diag}(e^{J_1 t}, \dots, e^{J_n t}) P^{-1} \mathbf{f}(0),$$

for some invertible matrix P of eigenvectors, with

$$e^{J_k t} = e^{-(1-\lambda_k^{\mathcal{A}})t} \begin{pmatrix} 1 & t & \dots & \frac{t^{m_k-1}}{(m_k-1)!} \\ & & & \vdots \\ & & & 1 \end{pmatrix},$$

where m_k are the eigenvalue multiplicities. Since by assumption G is connected and augmented with self-loops, the row-stochastic attention matrix \mathcal{A} computed in Chamberlain et al. [2021a] with softmax activation is *regular*, meaning that there exists $m \in \mathbb{N}$ such that $(\mathcal{A}^m)_{ij} > 0$ for each entry (i, j) . Accordingly, we can apply Perron Theorem to derive that any eigenvalue of \mathcal{A} has real part smaller than one except the eigenvalue $\lambda_0^{\mathcal{A}}$ with multiplicity one, associated with the Perron eigenvector $\mathbf{1}_n$. Accordingly, we find that each block $e^{J_k t}$ decays to zero as $t \rightarrow \infty$ with the exception of the one $e^{J_0 t}$ associated with the Perron eigenvector. In particular, the projection of \mathbf{f}_0 over the Perron eigenvector is just $\mu \mathbf{1}_n$, with μ the average of the feature initial condition. This completes the proof. \square

C.2 Common GNN architectures as gradient flow

We consider linear GNNs of the form

$$\mathbf{F}(t+1) = \mathbf{F}(t)\Omega + \mathcal{A}\mathbf{F}(t)\mathbf{W} + \beta\mathbf{F}(0)\tilde{\mathbf{W}}, \quad 0 \leq t \leq T.$$

If $\Omega = \mathbf{0}$, $\beta = 0$ and $\mathcal{A} = \bar{\mathbf{A}}$, we recover linear GCN with weights shared across layers Kipf and Welling [2017], Wu et al. [2019]. Similarly, if $\mathcal{A} = \bar{\mathbf{A}}$ and $\beta = 0$, this is linear GraphSAGE Hamilton et al. [2017] with propagation given by *symmetric* adjacency and weights shared across layers. A symmetric version of GAT Veličković et al. [2018] can be recovered if $\Omega = \mathbf{0}$, $\beta = 0$ and $\mathcal{A} = \bar{\mathbf{A}}$ is a *symmetric* attention matrix depending only on the initial encoded features – note that in general a row-stochastic matrix may not be symmetric so a *symmetrization of a row-stochastic attention matrix would generally fail to remain row-stochastic*. We believe that this point deserves further investigation. Finally GCNII Chen et al. [2020] can be recovered by taking $\Omega = \mathbf{0}$ and $\mathcal{A} = \bar{\mathbf{A}}$.

Proof of Lemma 4.2. This follows from the same argument in eq. (25) once we regard the linear system in eq. (13) as a unit step size Euler discretization

$$\dot{\mathbf{F}}(t) \sim \mathbf{F}(t+1) - \mathbf{F}(t) = \mathbf{F}(t)(\Omega - \mathbf{I}_d) + \mathcal{A}\mathbf{F}(t)\mathbf{W} + \beta\mathbf{F}(0)\tilde{\mathbf{W}}$$

\square

C.3 Spectral analysis of the channel-mixing: the discrete case

We first address the proof of the main result.

Proof of Theorem 4.3. We consider a linear dynamical system

$$\mathbf{F}(t+\tau) = \mathbf{F}(t) + \tau \bar{\mathbf{A}}\mathbf{F}(t)\mathbf{W},$$

with \mathbf{W} symmetric. We vectorize the system and rewrite it as

$$\text{vec}(\mathbf{F}(t+\tau)) = (\mathbf{I}_{nd} + \tau \mathbf{W} \otimes \bar{\mathbf{A}}) \text{vec}(\mathbf{F}(t))$$

which in particular leads to

$$\text{vec}(\mathbf{F}(m\tau)) = (\mathbf{I}_{nd} + \tau \mathbf{W} \otimes \bar{\mathbf{A}})^m \text{vec}(\mathbf{F}(0)).$$

We can then write explicitly the solution as

$$\text{vec}(\mathbf{F}(m\tau)) = \sum_{r,i} (1 + \tau \lambda_r^{\mathbf{W}} (1 - \lambda_i^{\Delta}))^m c_{r,i}(0) \phi_r^{\mathbf{W}} \otimes \phi_i^{\Delta}.$$

We now verify that by assumption in eq. (14) the dominant term of the solution is the projection into the eigenspace associated with the eigenvalue $\rho_- = |\lambda_-^{\mathbf{W}}|(\rho_{\Delta} - 1)$. The following argument follows the same structure in the proof of Proposition 3.1 with the extra condition given by the step-size. First, we note that for any r such that $\lambda_r^{\mathbf{W}} > 0$, we have

$$|1 + \tau \rho_-| > |1 + \tau \lambda_+^{\mathbf{W}}| \geq |1 + \tau \lambda_r^{\mathbf{W}} (1 - \lambda_i^{\Delta})|$$

since we required $\rho_- > \lambda_+^{\mathbf{W}}$ in eq. (14). Conversely, if $\lambda_r^{\mathbf{W}} < 0$, then

$$|1 + \tau \lambda_r^{\mathbf{W}} (1 - \lambda_i^{\Delta})| \leq \max\{|1 + \tau \rho_-|, |1 + \tau \lambda_-^{\mathbf{W}}|\}$$

Assume that $\tau |\lambda_-^{\mathbf{W}}| > 1$, otherwise there is nothing to prove. Then $|1 + \tau \rho_-| > \tau |\lambda_-^{\mathbf{W}}| - 1$ if and only if

$$\tau |\lambda_-^{\mathbf{W}}| (2 - \rho_{\Delta}) < 2,$$

which is precisely the right inequality in eq. (14). We can then argue exactly as in the proof of Proposition 3.1 to derive that for each index r such that $\lambda_r^{\mathbf{W}} < 0$ and $\lambda_r^{\mathbf{W}} \neq \lambda_-^{\mathbf{W}}$, then

$$|1 + \tau \lambda_r^{\mathbf{W}} (1 - \lambda_i^{\Delta})| \leq \max\{|1 + \tau |\lambda_{-,2}^{\mathbf{W}}|(\rho_{\Delta} - 1)|, |1 + \tau |\lambda_-^{\mathbf{W}}|(\lambda_{n-2}^{\Delta} - 1)|\}$$

with $\lambda_{-,2}^{\mathbf{W}}$ and λ_{n-2}^{Δ} defined in eq. (26). We can then introduce

$$\delta_{\text{HFD}} := \max\{\lambda_+^{\mathbf{W}}, \rho_- - |\lambda_-^{\mathbf{W}}| \text{gap}(\rho_{\Delta} \mathbf{I} - \Delta), \rho_- - (\rho_{\Delta} - 1) \text{gap}(|\lambda_-^{\mathbf{W}}| \mathbf{I} + \mathbf{W}), |\lambda_-^{\mathbf{W}}| - \frac{2}{\tau}\} \quad (29)$$

and conclude that

$$\begin{aligned} \mathcal{E}^{\text{Dir}}(\mathbf{F}(t)) &= \frac{1}{2} \sum_{r,i} (1 + \tau \lambda_r^{\mathbf{W}} (1 - \lambda_i^{\Delta}))^{2m} c_{r,i}^2(0) \lambda_i^{\Delta} \\ &= (1 + \tau \rho_-)^{2m} \left(\frac{\rho_{\Delta}}{2} \sum_{r:\lambda_r^{\mathbf{W}}=\lambda_-^{\mathbf{W}}} c_{r,\rho_{\Delta}}^2(0) + \mathcal{O}\left(\left(\frac{1 + \tau \delta_{\text{HFD}}}{1 + \tau \rho_-}\right)^{2m}\right) \sum_{i:r:\lambda_r^{\mathbf{W}}(1-\lambda_i^{\Delta})\neq\rho_-} c_{r,i}^2(0) \lambda_i^{\Delta} \right) \\ &= (1 + \tau \rho_-)^{2m} \left(\frac{\rho_{\Delta}}{2} \|P_{\mathbf{W}}^{\rho_-} \mathbf{F}(0)\|^2 + \mathcal{O}\left(\left(\frac{1 + \tau \delta_{\text{HFD}}}{1 + \tau \rho_-}\right)^{2m}\right) \right). \end{aligned}$$

In particular, we can normalize the solution and due to $(\mathbf{I}_d \otimes \Delta) P_{\mathbf{W}}^{\rho_-} \text{vec}(\mathbf{F}(0)) = \rho_{\Delta} P_{\mathbf{W}}^{\rho_-} \text{vec}(\mathbf{F}(0))$, we complete the proof for the case with residual connection.

If instead we drop the residual connection and simply consider $\dot{\mathbf{F}}(t) = \bar{\mathbf{A}} \mathbf{F}(t) \mathbf{W}$, then

$$\text{vec}(\mathbf{F}(m\tau)) = (\tau \mathbf{W} \otimes \bar{\mathbf{A}})^m \text{vec}(\mathbf{F}(0)).$$

Since \mathbf{G} is not bipartite, the Laplacian spectral radius satisfies $\rho_{\Delta} < 2$. Therefore, for each pair of indices (r, i) we have the following bound:

$$|\lambda_r^{\mathbf{W}} (1 - \lambda_i^{\Delta})| \leq \max\{\lambda_+^{\mathbf{W}}, |\lambda_-^{\mathbf{W}}|\},$$

and the inequality becomes strict if $i > 0$, i.e. $\lambda_i^{\Delta} > 0$. The eigenvalues $\lambda_+^{\mathbf{W}}$ and $\lambda_-^{\mathbf{W}}$ are attained along the eigenvectors $\phi_+^{\mathbf{W}} \otimes \phi_0^{\Delta}$ and $\phi_-^{\mathbf{W}} \otimes \phi_0^{\Delta}$ respectively. Accordingly, the dominant terms of the evolution lie in the kernel of $\mathbf{I}_d \otimes \Delta$, meaning that for any \mathbf{F}_0 with non-zero projection in $\ker(\mathbf{I}_d \otimes \Delta)$ – which is satisfied by all initial conditions except those belonging to a lower dimensional subspace – the dynamics is LFD. In fact, without loss of generality assume that $|\lambda_-^{\mathbf{W}}| > \lambda_+^{\mathbf{W}}$, then

$$\begin{aligned} \text{vec}(\mathbf{F}(m\tau)) &= |\lambda_-^{\mathbf{W}}|^m \sum_{r:\lambda_r^{\mathbf{W}}=\lambda_-^{\mathbf{W}}} (-1)^m c_{r,0}(0) \phi_-^{\mathbf{W}} \otimes \phi_0^{\Delta} \\ &\quad + |\lambda_-^{\mathbf{W}}|^m \left(\mathcal{O}(\varphi(m)) \left(\mathbf{I}_{nd} - \sum_{r:\lambda_r^{\mathbf{W}}=\lambda_-^{\mathbf{W}}} (\phi_-^{\mathbf{W}} \otimes \phi_0^{\Delta})(\phi_-^{\mathbf{W}} \otimes \phi_0^{\Delta})^{\top} \right) \text{vec}(\mathbf{F}(0)) \right), \end{aligned}$$

with $\varphi(m) \rightarrow 0$ as $m \rightarrow \infty$, which completes the proof. \square

We dedicate the end of this section to reformulating the gradient flow system $\mathbf{F}(t + \tau) = \mathbf{F}(t) + \tau \bar{\mathbf{A}}\mathbf{F}(t)\mathbf{W}$ explicitly in spectral form. If we write $\mathbf{\Delta} = \mathbf{U}\mathbf{\Lambda}\mathbf{U}^\top$ for the eigendecomposition of the graph Laplacian, Equation (15) follows immediately by

$$\mathbf{f}^r(t + \tau) = \mathbf{f}^r(t) + \tau \sum_{q=1}^d W_{rq}(\bar{\mathbf{A}}\mathbf{f}^q(t)) = \mathbf{f}^r(t) + \tau \sum_{q=1}^d W_{rq}(\mathbf{U}(\mathbf{I}_n - \mathbf{\Lambda})\mathbf{U}^\top \mathbf{f}^q(t)).$$

In particular, if we set $z_i^r(t) = \langle \mathbf{f}_i(t), \phi_r^{\mathbf{W}} \rangle$, then

$$\begin{aligned} z_i^r(t + \tau) &= \langle \mathbf{f}_i(t + \tau), \phi_r^{\mathbf{W}} \rangle = \langle \mathbf{f}_i(t) + \mathbf{W}(\bar{\mathbf{A}}\mathbf{f}(t))_i, \phi_r^{\mathbf{W}} \rangle \\ &= z_i^r(t) + \lambda_r^{\mathbf{W}} \sum_j \bar{a}_{ij} z_j^r(t), \end{aligned}$$

which concludes the derivation of eq. (16).

D Additional details on experiments

D.1 Additional details on GRAFF

Given a gradient flow dynamical system of the form $\mathbf{F}(t + \tau) = \mathbf{F}(t) + \tau \bar{\mathbf{A}}\mathbf{F}(t)\mathbf{W}$, the vectorized solution is

$$\text{vec}(\mathbf{F}(m\tau)) = \sum_{r,i} (1 + \tau \lambda_r^{\mathbf{W}}(1 - \lambda_i^{\mathbf{\Delta}}))^m c_{r,i}(0) \phi_r^{\mathbf{W}} \otimes \phi_i^{\mathbf{\Delta}}.$$

We then see that the number of layers m – which coincides with the quotient of the integration time T by the step size τ – represents the degree of the polynomial computing the solution. More precisely, on a heterophilic graph for which a HFD dynamics is more suited than an LFD dynamics, the negative eigenvalues of \mathbf{W} are needed to magnify the graph high-frequencies. This in turn yields terms $(1 + \tau \lambda_r^{\mathbf{W}}(1 - \lambda_i^{\mathbf{\Delta}}))^m$ that would become unbounded with m growing if there is sufficient mass on the negative side of $\text{spec}(\mathbf{W})$. On the other hand, terms associated with positive eigenvalues of \mathbf{W} would quickly lead to over-smoothing. One then expects that on heterophilic graphs the degree m of the polynomial – i.e. the *number of layers* – should be generally smaller than that on homophilic graphs. This is confirmed in our real-world experiments where on the larger heterophilic graphs like Squirrel and Chameleon the optimal number m is an integer in $\{2, 3, 4\}$.

D.2 General Experimental details

GRAFF is implemented in PyTorch [Paszke et al. \[2019\]](#), using PyTorch geometric [Fey and Lenssen \[2019\]](#) and torchdiffEq [Chen et al. \[2018\]](#). Code and instructions to reproduce the experiments are available on GitHub. Hyperparameters were tuned using wandb [Biewald \[2020\]](#) and random grid search. Experiments were run on AWS p2.8xlarge machines, each with 8 Tesla V100-SXM2 GPUs.

D.3 Additional details on synthetic ablation studies:

The synthetic Cora dataset is provided by [\[Zhu et al., 2020, Appendix G\]](#). They use a modified preferential attachment process to generate graphs for target levels of homophily. Nodes, edges and features are sampled from Cora proportional to a mix of class compatibility and node degree resulting in a graph with the required homophily and appropriate feature/label distribution. To validate the provided data before use we provide table 2 summarising the properties of the synthetic Cora dataset. All rows/levels of homophily have the same number of nodes (1,490), edges (5,936), features (1,433) and classes (5).

As well as the ablation shown in fig. 2 we used this dataset to perform an ablation using GCN as the baseline. We assess the impact of each of the steps necessary to augment a standard GCN model to GRAFF. This involves 5 steps; 1) add an encoder/decoder. 2) add a residual connection. 3) share the weights of \mathbf{W} and $\mathbf{\Omega}$ across time/layers. 4) symmetrize \mathbf{W} and $\mathbf{\Omega}$. 5) remove the non-linearity between layers. The results are shown in fig. 3 and corroborate Theorem 4.3 that adding a residual term is beneficial especially in low-homophily scenarios. We also note augmentations 3,4 and 5 are not "costly" in terms of performance.

homophily	max_degree	min_degree	av_degree	density	edge_homoph	node_homoph
0.00	84.33	1.67	3.98	0.0027	0.00	0.00
0.10	71.33	2.00	3.98	0.0027	0.10	0.10
0.20	73.33	1.67	3.98	0.0027	0.20	0.20
0.30	70.00	2.00	3.98	0.0027	0.29	0.30
0.40	77.67	2.00	3.98	0.0027	0.39	0.39
0.50	76.33	2.00	3.98	0.0027	0.49	0.49
0.60	76.00	1.67	3.98	0.0027	0.59	0.60
0.70	67.67	2.00	3.98	0.0027	0.70	0.70
0.80	58.00	1.67	3.98	0.0027	0.78	0.79
0.90	58.00	1.67	3.98	0.0027	0.89	0.89
1.00	51.00	2.00	3.98	0.0027	1.00	1.00

Table 2: Summary of properties of synthetic Cora dataset

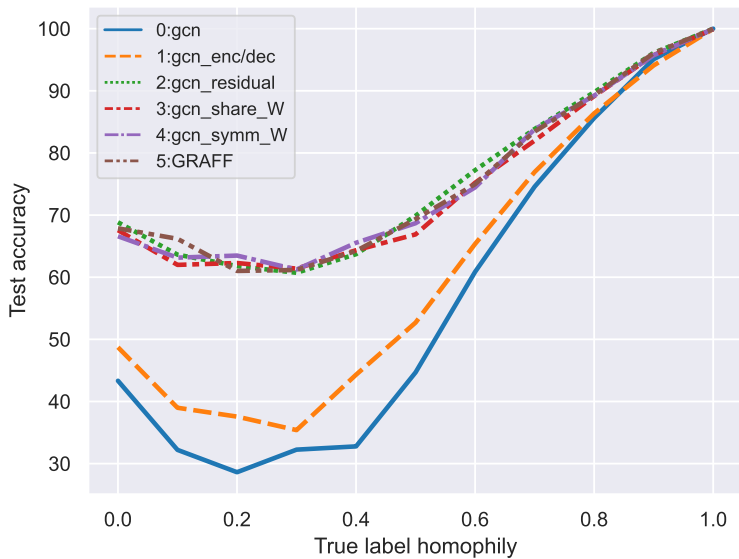


Figure 3: Experiments on synthetic Cora - GCN ablation

D.4 Additional details on real-world ablation studies

For the real-world experiments in table 1 we performed 10 repetitions over the splits taken from Pei et al. [2020]. For all datasets we used the largest connected component (LCC) apart from Citeseer where the 5th and 6th split are LCC and others require the full dataset. For Chameleon and Squirrel we added self loops and made the edges undirected as a preprocessing step. All other datasets are provided as undirected but without self loops. Each split uses 48/32/20 of nodes for training, validation and test set respectively. Table 3 summarises each of the datasets.

We used the real-world datasets to perform 2 ablation studies. First we choose 2 heterophilic datasets (Chameleon, Squirrel) and 2 homophilic (Cora, Citeseer) and observed how the size of the hidden dimension effected performance for the structures of \mathbf{W} described in section 5. For heterophilic datasets we used the splits from Pei et al. [2020]. For homophilic datasets we used the methodology in Shchur et al. [2018], each split randomly selects 1,500 nodes for the development set, from the development set 20 nodes for each class are taken as the training set, the remainder are allocated as the validation set. The remaining nodes outside of the development set are used as the test set. This gives a lower percentage (3-6%) of training nodes. This approach was taken because less training information is needed in the homophilic setting and performance can become less sensitive to other factors, meaning less signal from the controlled variable. From fig. 4 we see that (DD) is more

dataset	nodes	edges	features	classes	max_degree	min_degree	av_degree	density	edge_homoph	node_homoph
Texas	183	558	1,703	5	104	1	3.05	0.0167	0.06	0.06
Wisconsin	251	900	1,703	5	122	1	3.59	0.0143	0.18	0.16
Cornell	183	554	1,703	5	94	1	3.03	0.0165	0.3	0.3
Film	7,600	53,318	932	5	1,303	1	7.02	0.0009	0.22	0.22
Squirrel	5,201	401,907	2,089	5	1,904	2	77.27	0.0149	0.23	0.29
Chameleon	2,277	65,019	2,325	5	733	2	28.55	0.0125	0.26	0.33
Citeseer *	3,327	9,104	3,703	6	99	0	2.74	0.0008	0.74	0.71
Citeseer	2,120	7,358	3,703	6	99	1	3.47	0.0016	0.73	0.71
Pubmed	19,717	88,648	500	3	171	1	4.5	0.0002	0.8	0.79
Cora	2,485	10,138	1,433	7	168	1	4.08	0.0016	0.8	0.81

Table 3: Summary of properties of real-word datasets. All LCC except *

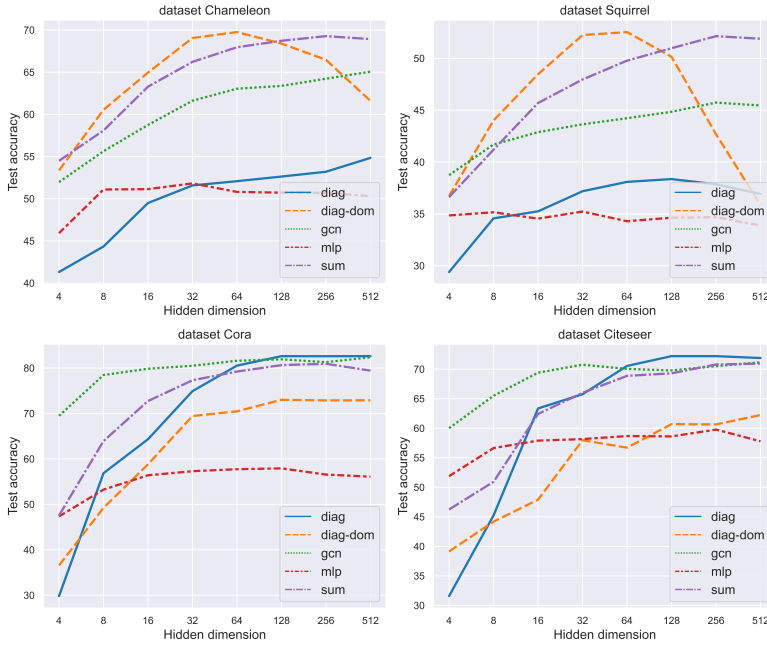


Figure 4: Ablation against hidden dimension

parameter efficient than *sum* in the heterophilic setting and (D) (a parameter light configuration) outperforms in the homophilic setting.

The second ablation study further corroborates the behaviour seen in fig. 2. We tested the structures of \mathbf{W} against the real-world datasets with known homophily, again *neg-prod* outperforms *prod* in the heterophilic setting and vice-versa due the sign of their spectra.

dataset	neg_prod	prod	sum
Chameleon	67.32	58.86	68.36
Squirrel	51.39	42.11	51.29
Cora	31.80	79.65	81.17
Citeseer	32.47	67.31	67.53

Table 4: Ablation with controlled spectrum of \mathbf{W} on real-world datasets

To validate the complexity analysis in Section 5 we performed a runtime ablation for the models between standard GCN and GRAFF described in the GCN ablation Figure 3. The average inference runtime over 100 runs for 1 split of Cora was recorded. We also include runtimes for the provided dense and sparse implementations of GGCN Yan et al. [2021]. Adding the encoder/decoder (step 1) speeds up the model due to dimensionality reduction. Subsequent steps also reduce complexity and offer speedup with GRAFF performing the fastest.

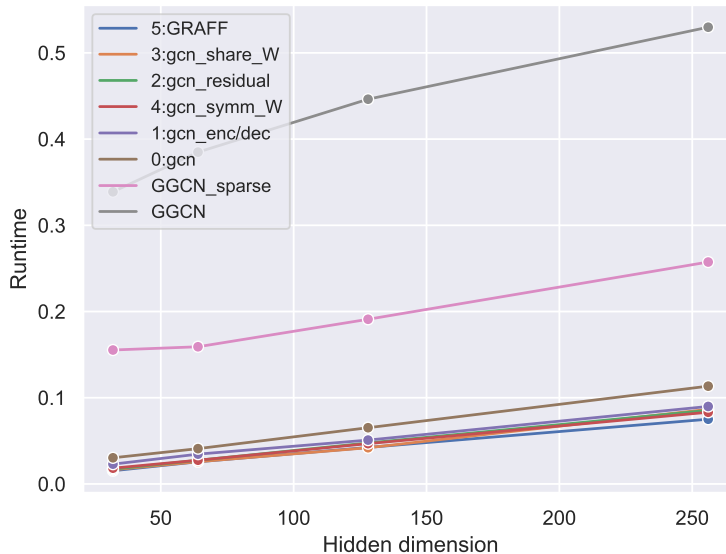


Figure 5: Runtime ablation for inference on Cora dataset

D.5 Details on hyperparameters

Using wandb [Biewald \[2020\]](#) we performed a random grid search with uniform sampling of the continuous variables. We provide the hyperparameters that achieved the best results from the random grid search in table 5. An implementation that uses these hyperparameters is available in the provided code with hyperparameters provided in `graf_f_params.py`. Input dropout and dropout are the rates applied to the encoder/decoder respectively *with no dropout applied in the ODE block*.

	w_style	lr	decay	dropout	input_dropout	hidden_dim	time	step_size
chameleon	diag_dom	0.0014	0.0004	0.37	0.43	64	3.2	1
squirrel	diag_dom	0.0058	0.0002	0.50	0.51	64	2.3	1
texas	diag_dom	0.0041	0.0354	0.33	0.39	64	0.6	0.5
wisconsin	diag	0.0029	0.0318	0.37	0.37	64	2.1	0.5
cornell	diag	0.0021	0.0184	0.30	0.44	64	2.0	1
film	diag	0.0026	0.0130	0.48	0.42	64	1.5	1
Cora	diag	0.0026	0.0413	0.34	0.53	64	3.0	0.25
Citeseer	diag	0.0001	0.0274	0.22	0.51	64	2.0	0.5
Pubmed	diag	0.0039	0.0003	0.42	0.41	64	2.6	0.5

Table 5: Selected hyperparameters for real-world datasets